MASARYKOVA UNIVERZITA
Přírodovědecká fakulta
Ústav Teoretické Fyziky a Astrofyziky

Bakalářská práce

Brno 2026 **Samuel Adámek**

MASARYKOVA
UNIVERZITA
PŘÍRODOVĚDECKÁ FAKULTA
ÚSTAV TEORETICKÉ FYZIKY A ASTROFYZIKY

Vývoj charakteristické frekvence rychlé variability trpaslič novy V1504 Cyg během přechodu ze vzplanutí do klidného stadia

Bakalářská práce

Samuel Adámek

Vedoucí práce: Mgr. Andrej Dobrotka, PhD. **Brno 2026**

Bibliografický záznam

Autor:	Samuel Adámek Přírodovědecká fakulta, Masarykova univerzita Ústav Teoretické Fyziky a Astrofyziky
Název práce:	Vývoj charakteristické frekvence rychlé variability trpasličí novy V1504 Cyg během přechodu ze vzplanutí do klidného stadia
Studijní program:	Fyzika
Studijní obor:	Astrofyzika
Vedoucí práce:	Mgr. Andrej Dobrotka, PhD.
Akademický rok:	2025/2026
Počet stran:	xv + 46
Klíčová slova:	kataklyzmické proměnné; trpasličí novy; akreční disky; PDS; flickering; Kepler; V1504 Cyg

Bibliographic Entry

Author:	Samuel Adámek Faculty of Science, Masaryk University Department of Theoretical Physics and Astrophysics
Title of Thesis:	Evolution of the characteristic frequency of the fast variability of dwarf nova V1504 Cyg during transition from outburst to quiescence
Degree Programme:	Physics
Field of Study:	Astrophysics
Supervisor:	Mgr. Andrej Dobrotka, PhD.
Academic Year:	2025/2026
Number of Pages:	$\mathrm{xv} + 46$
Keywords:	cataclysmic variables; dwarf novae; accretion discs; PDS; flickering; Kepler; V1504 Cyg

Abstrakt

V této bakalářské práci analyzujeme vývoj charakteristické frekvence rychlé variability trpasličí novy typu SU UMa V1504 Cyg během přechodu ze vzplanutí do klidového stadia s využitím dat z družice *Kepler* s režimem krátké kadence (58,8 s). Ze 112 vybraných vzplanutí extrahujeme charakteristické frekvence v 19 časových intervalech pokrývajících 4,75 dne pomocí dvou nezávislých metod: PDS analýzy a metody AFP. Oba přístupy poskytují shodný výsledek: charakteristická frekvence plynule klesá z $\sim$1,8 mHz v blízkosti maxima vzplanutí na $\sim$0,4 mHz v klidovém stadiu, bez jakékoliv nespojitosti. Tento výsledek vylučuje scénář, ve kterém se střídají víceré nezávislé zdroje variability, a naopak ukazuje, že se jeden zdroj plynule vyvíjí společně s přechodem akrečního disku mezi stavy. Shoda mezi výsledky PDS a AFP potvrzuje nestandardní metodu AFP jako komplementární nástroj pro sledování vývoje frekvencí. Porovnání s dynamickou časovou škálou umístilo pozorované frekvence do střední až vnější části disku, zatímco výpočet viskózní časové škály přiřadil frekvenci ve vzplanutí k vnitřním oblastem disku, v souladu s nedávnými numerickými simulacemi modelu diskové nestability. Ani jedna z interpretací plně nevysvětluje pozorovaný vývoj a fyzikální mechanismus způsobující pokles frekvence teda zůstává otevřený.

Abstract

In this thesis, we analyze the evolution of the characteristic flickering frequency of the SU UMa-type dwarf nova V1504 Cyg during the transition from outburst to quiescence, using *Kepler* satellite data in short-cadence mode (58.8 s). From 112 selected outbursts, we extract characteristic frequencies in 19 time Bins spanning 4.75 days using two independent methods: power density spectrum (PDS) analysis and the averaged flare profile (AFP) method. Both methods yield a consistent result: the characteristic frequency declines smoothly from $\sim$1.8 mHz near the outburst peak to $\sim$0.4 mHz in quiescence, with no discontinuity at any stage. This rules out the scenario in which multiple independent variability sources alternate dominance, and instead indicates that a single source evolves continuously as the accretion disc transitions between states. The agreement between the PDS and AFP results validates the non-standard AFP method as a complementary tool for tracking frequency evolution. A comparison with the dynamical timescale placed the observed frequencies at mid-to-outer disc radii, while a viscous timescale calculation mapped the outburst peak frequency to the inner disc, consistent with recent numerical simulations of the disc instability model. Neither interpretation fully explains the observed evolution, and the physical mechanism driving the frequency decline remains an open question.

MASARYKOVA UNIVERZITA
PŘÍRODOVĚDECKÁ FAKULTA
KOTLÁŘSKÁ 2, 611 37 BRNO
IČ: 00216224
DIČ: CZ00216224

ZADÁNÍ BAKALÁŘSKÉ PRÁCE

Akademický rok: 2025/2026

Ústav:	Ústav teoretické fyziky a astrofyziky
Student:	Samuel Adámek
Program:	Fyzika
Specializace:	Astrofyzika

Ředitel *ústavu* PřF MU Vám ve smyslu Studijního a zkušebního řádu MU určuje bakalářskou práci s názvem:

Název práce:	Vývoj charakteristické frekvence rychlé variability trpasličí novy V1504 Cyg během přechodu ze vzplanutí do klidného stadia
Název práce anglicky:	Evolution of the characteristic frequency of the fast variability of dwarf nova V1504 Cyg during transition from outburst to quiescence
Jazyk práce:	angličtina

Oficiální zadání:
Cataclysmic variables show rapid variability that characterizes the accretion process. From the results so far, we know that the characteristic frequencies of such variability depend on the stage of activity. While during the outburst of a dwarf nova V1504 Cyg the 1 mHz frequency is dominant, in the quiescence a lower frequency around 0.4 mHz is evident. The aim of the work is to obtain a smooth course of frequency change using data from the Kepler satellite and to determine whether the 1 mHz signal disappears and a still-present signal around 0.4 mHz appears, or the frequency smoothly changes from 1 mHz to 0.4 mHz. Both cases lead to different interpretations and localization of the source of the rapid variability.

Vedoucí práce:	Mgr. Andrej Dobrotka, PhD.
Datum zadání práce:	17. 11. 2025
V Brně dne:	24. 4. 2026

Zadání bylo schváleno prostřednictvím IS MU.

Samuel Adámek, 15. 12. 2025
Mgr. Andrej Dobrotka, PhD., 15. 12. 2025
RNDr. Luboš Poláček, 15. 12. 2025

Poděkování

V prvom rade by som sa chcel poďakovať Mgr. Andrejovi Dobrotkovi, PhD. za všetku jeho ochotu, čas a cenné rady pri zhotovovaní tejto práce napriek dištančným obmedzeniam, ako aj za oboznámenie ma s ďalšou vetvou astrofyziky. Tiež by som sa rád poďakoval Ing. Jozefovi Magdolénovi za technické rady. Nakoniec prejavujem vďaku aj mojej rodine a priateľke za neustálu podporu počas štúdia.

Prohlášení

Prohlašuji, že jsem svoji bakalářskou práci vypracoval samostatně pod vedením vedoucího práce s využitím informačních zdrojů, které jsou v práci citovány.

Brno 2026

. . . . . .

Samuel Adámek

Contents

Introduction

Cataclysmic variable stars (CVs) are close binary systems in which a white dwarf accretes matter from a low-mass companion, typically a late-type main-sequence star. This accretion process leads to a wide variety of photometric phenomena, including outbursts, quasi-periodic oscillations, and stochastic oscillations (e.g., Knigge et al. 2011; Scaringi 2014). Subdividing CVs by their variability characteristics, dwarf novae are systems with quasi-regular outbursts lasting days, separated by a quiescent state that can last weeks. These outbursts are caused by thermal-viscous instabilities in the disc, commonly described by the disc instability model (Lasota 2001).

While the global properties of dwarf nova outbursts have been extensively studied, high-cadence observations reveal that these systems also exhibit rapid stochastic variability known as "flickering" (see Warner 1995 for a review). The currently accepted interpretation is that flickering originates from turbulence and local instabilities in the accretion disc, therefore providing insight into the mechanisms that govern the accretion process. Studies of this variability often rely on power density spectrum (PDS) analysis, where characteristic frequencies may be identified as Lorentzian components or breaks in a broken power-law model.

In this thesis, we focus on the dwarf nova V1504 Cyg, using photometric data collected by the *Kepler* satellite. Along with the conventional PDS analysis, we apply the average flare profile (AFP) method. First proposed by Negoro et al. (1994) for the analysis of *Ginga* data of Cygnus X-1, the AFP method constructs an average profile of superimposed flares, providing a complementary view of the variability morphology and signature timescales. Using these approaches, we extract characteristic frequencies associated with flickering during the transition from outburst to quiescence.

The goals of this work are as follows. First, to make use of high-quality photometric data by implementing two independent methods for a dwarf nova system to describe the fast variability of V1504 Cyg. Second, interpreting the characteristic frequency evolution from a high state to a low state, we try to shine light on the physical processes behind such behaviour. Specifically, whether a single variability source evolves continuously as the system transitions between states, or, whether multiple independent sources are present, each dominant in a different activity stage.

The thesis is structured as follows. Chapter 1 presents the theoretical background, including accretion processes, close binary systems, the structure and phenomenology of dwarf novae, and a discussion of flickering. Chapter 2 focuses on the data and methods. We describe the handling of *Kepler* observations of V1504 Cyg, followed by an implementation of the PDS and AFP methods. Chapter 3 presents the results, detailing the extracted characteristic frequencies and the variability morphology. Finally, Chapter 4 provides the

discussion and possible interpretations. We finish off with a summary of our findings in Chapter 5.

Chapter 1

Accreting Binary Systems

1.1 Accretion

Accretion is a fundamental physical process that is observed on a vast range of scales and is responsible for powering some of the most luminous phenomena in the universe. From still forming young stellar objects to massive active galactic nuclei, it functions as an indispensable gateway for the study of our universe. Accretion refers to the gravitational capture of matter by a compact or massive object, during which gravitational potential energy is converted into kinetic energy and subsequently radiated away.

Accretion Origin

In interacting binary systems, which are the focus of this thesis, accretion is enabled by mass-transfer from one component to the other, which may occur at different stages of the binary's evolution. There are two main mechanisms by which such mass-transfer can take place. In the first case, the donor star expands during its evolution, or the orbital separation of the system decreases, until its outer layers fill the Roche lobe. Matter is then transferred through the inner Lagrange point toward the companion, a process known as Roche-lobe overflow. Alternatively, mass-transfer may occur through stellar wind accretion, in which one component loses a significant fraction of its mass via a radiatively driven wind, part of which is captured by the companion (see e.g., Frank et al. 2002 for a review).

In both accretion scenarios, the transferred material carries non-zero angular momentum with respect to the accreting object. As a result, the inflowing matter cannot fall directly along a radial path and instead settles into a rotating accretion disc. Within this disc, matter follows approximately Keplerian orbits around the central object. It gradually loses angular momentum and spirals inward, ultimately accreting onto the surface of the central star.

Angular Momentum Transport

After accretion is established, it itself, however, cannot proceed if the disc lacks an efficient mechanism for angular momentum transport. Without it, the disc would remain in a stable rotational configuration, and accretion onto the central object would stop. In a Keplerian

disc, we can write the specific angular momentum h of the orbiting material in circular orbit as

$$h = \frac{L}{m} = R^2 \sqrt{\frac{GM}{R^3}} \propto \sqrt{R}, \tag{1.1}$$

where L is the angular momentum, m is the mass of the material, M is the mass of the central object, G is the gravitational constant and $\sqrt{GM}/\sqrt{R^3}$ is the Keplerian angular velocity Ω_K. As we see, h increases with radial distance from the central object R. Then, for matter to spiral inward, its excess angular momentum must be transferred outward to larger disc radii and be removed from the disc.

The α-Prescription and Turbulence

Early considerations by Shakura & Sunyaev (1973) showed that sources of angular momentum loss (AML), such as microscopic viscosity or AML by radiation, are far too weak to account for the observed accretion rates in astrophysical systems. The corresponding viscous timescales would exceed the evolutionary timescales of accreting binaries, which renders accretion inefficient. The authors concluded that the dominant AML mechanisms are caused by magnetic fields and turbulence. They introduced the now famous α-prescription, which parametrizes the effective kinematic viscosity ν in terms of local disc properties:

$$\nu = \alpha c_s H, \tag{1.2}$$

where c_s is the speed of sound, H is the disc scale height given by the ratio of the horizontal disc height to its radius, and α is a dimensionless parameter expected to satisfy $\alpha \leq 1$. Equation 1.2 is simply a parametrization; it isolates all ignorance about the underlying viscosity mechanism into the single parameter α. Still, the α-prescription provides a possibility to compare theoretical models with observation. Nowadays, it is widely accepted that the main source of turbulence in a Keplerian disc is magnetohydrodynamic turbulence, more specifically, magneto-rotational Balbus-Hawley instability (e.g., Balbus & Hawley 1998; Balbus 2005; Ji et al. 2006). It is also important to state that the Shakura-Sunyaev disc is a global solution. The assumption that the mass accretion rate is constant with radius is not necessarily true due to two factors. Hydrogen ionization plays an important role at low luminosities, while radiation pressure should have an effect at higher luminosities (see Done et al. 2007).

Accretion Disc Structure

We have seen that systems containing accreting material with sufficient angular momentum result in an accretion disc. In many of these systems, the flow of matter is so closely constricted to the orbital plane, that we can consider the disc a two-dimensional flow of gas. This first order approximation, also known as the *thin disc approximation* which we can write as $H \ll R$, has successfully reproduced observations of close binary systems.

The structure of a thin disc can be described in terms of its surface density $\Sigma(R)$, defined as the mass per unit surface area of the disc. In addition to the radial variation of surface density, accretion discs have inner and outer boundaries that can be physically determined.

At the inner edge of the disc, the accreting material must decelerate from its Keplerian orbital velocity to match the much slower rotation of the stellar surface. This transition occurs in a narrow region known as the *boundary layer*, where kinetic energy is converted into thermal energy and radiated away (Warner 1995). During outburst, the boundary layer is optically thick and emits primarily soft X-rays and in the extreme ultraviolet, while during quiescence it becomes optically thin and emits hard X-rays. The inner disc therefore does not extend exactly to the stellar surface, though this distinction can be neglected in approximation. The disc can also be truncated further out as a result of evaporation or magnetic interaction. The outer radius is often set by tidal interactions with the companion star in a binary system (Lasota 2001).

Accretion Timescales

Accretion discs are governed by several characteristic timescales, each associated with a different physical process. These timescales determine how rapidly the disc can respond to perturbations. In general, the characteristic timescales depend on the radial distance from the central object (Frank et al. 2002).

The shortest relevant timescale is the dynamical (orbital) timescale, corresponding to the period of Keplerian motion of matter at a given disc radius. It is given by

$$t_{\rm dyn} \sim \Omega_K^{-1} = \sqrt{\frac{R^3}{GM}}, \tag{1.3}$$

This timescale characterizes the fastest processes in the disc and sets a lower limit on variability timescales associated with orbital motion (Frank et al. 2002).

On longer timescales, the disc evolves thermally. The thermal (Kelvin-Helmholtz) timescale describes the time required for the disc to radiate away its internal energy and reach thermal equilibrium following a perturbation. It is related to the dynamical timescale through

$$t_{\rm th} \sim \frac{1}{\alpha} t_{\rm dyn}. \tag{1.4}$$

Since $\alpha < 1$, the thermal timescale is typically longer than the dynamical timescale, but still significantly shorter than the timescale on which mass is transported through the disc (Shakura & Sunyaev 1973; Frank et al. 2002).

The longest and most important timescale for accretion is the viscous timescale, which governs the radial transport of mass and angular momentum through the disc. It can be expressed as

$$t_{\rm visc} \sim \frac{R^2}{\nu}. \tag{1.5}$$

Using the α-prescription, the viscous timescale for a thin disc can be written as

$$t_{\rm visc} \sim \frac{1}{\alpha} \left(\frac{R}{H}\right)^2 t_{\rm dyn}, \tag{1.6}$$

showing that viscous evolution is much slower than both dynamical and thermal processes (see Frank et al. 2002 for a review).

These timescales imply that accretion discs can exhibit variability over a broad range of temporal frequencies. Rapid fluctuations originate in the hot, inner disc regions and slower variations are connected with the cooler, outer disc structure. The correspondence between dynamical, thermal, and viscous processes provides an opportunity for interpreting the observed variability in interacting binary systems.

1.2 Close Binary Systems

Close binary systems consist of two stars orbiting sufficiently near to each other that their mutual gravitational interaction strongly influences their evolution. These systems are broadly classified based on the interaction between their components. In detached systems, neither star fills its Roche lobe and no mass transfer occurs. In contact systems, both components overflow their Roche lobes and share a common envelope. In semi-detached systems, one component fills its Roche lobe and transfers mass to the other through the inner Lagrange point, leading to accretion. It is this last class that is relevant to our work. The nature of the accreting primary largely determines the observational properties of the system, and therefore, semi-detached systems can be divided into two classes: cataclysmic variables (CVs), in which the primary is a white dwarf, and low-mass X-ray binary transients (LMXBTs), in which the primary is either a neutron star or a black hole (see Warner 1995 for a review).

Low-Mass X-ray Binary Transients

These systems typically have orbital periods ranging from a few hours to several days. During active phases, the accretor releases large amounts of energy, resulting in emission dominated by high-energy X-rays and placing LMXBTs among the brightest Galactic X-ray sources.

The accretion flow in LMXBTs is commonly described by a geometry consisting of an optically thick, geometrically thin accretion disc at large radii and a hot, optically thin inner flow closer to the primary. At high accretion rates, the disc is thought to extend down to the innermost stable circular orbit, mainly producing a soft X-ray component. At lower luminosities, evidence suggests that the inner disc is truncated and replaced by a hot, radiatively inefficient flow, which gives rise to hard X-ray emission via Comptonization. This hot inner region is also believed to play a key role in the formation of relativistic jets observed in many systems (see Done et al. 2007 for a review).

A defining observational characteristic of LMXBTs is their transient nature. These systems spend most of their time in a quiescent state with low X-ray luminosity, contrasted by episodic outbursts during which the luminosity increases by several orders of magnitude. The X-ray and optical light curves of these outbursts display a typical rapid rise followed by an approximately exponential decay. In many cases, secondary maxima or rebrightenings are observed during the decay phase. The decay shape can be naturally explained by a thermal-viscous instability operating in the accretion disc while the secondary maxima are possibly linked to irradiation. In such a case, strong radiation emitted from the disc affects the donor star, causing bloating, thereby modifying the mass-transfer rate and disc structure (Chen et al. 1997).

Cataclysmic Variable Stars

The observational and physical properties of CVs are largely determined by the mass-transfer rate and the characteristics of the white dwarf, including its magnetic field. We know that most CVs are magnetic to an extent, but in many systems the field strength is sufficiently weak that it does not significantly affect the accretion disc. These are the sub-type of non-magnetic CVs. Magnetic CVs are systems with stronger fields, further classified as polars or intermediate polars, in which the magnetic field channels the accretion flow directly onto the magnetic poles, suppressing or truncating the inner disc (Warner 1995).

Another division of CVs is based upon the behaviour of their accretion discs and properties. The presence, amplitude, and recurrence of optical outbursts classifies non-magnetic CVs as either dwarf novae or nova-likes. These subclasses will be discussed in the subsequent section.

The orbital periods of CVs span from roughly 80 minutes to about 12 hours, but their distribution is not uniform. There exists a deficit of systems between approximately 2 and 3 hours, known as the *period gap*. The observed period distribution is shown in Fig. 1.5. This gap is understood as a consequence of changes in the AML mechanism. Above the period gap, AML is dominated by magnetic braking, in which a magnetized stellar wind from the donor carries away angular momentum that is transferred from the orbit via tidal locking (Rappaport et al. 1982). Below the gap, the donor becomes fully convective and magnetic braking weakens, leaving gravitational radiation as the primary AML mechanism (Spruit & Ritter 1983). Unlike local disc viscosity, which is described by the α-prescription, these processes operate on the binary orbit and drive the long-term mass-transfer. As a result, systems temporarily detach and evolve through the gap with little or no mass-transfer (Knigge et al. 2011).

Although CVs and LMXBTs differ in the nature of their accretors, they share several similarities. Both can exhibit disc truncation, irradiation-driven modifications to the donor or disc, and AML affecting long-term evolution. In CVs, these processes manifest primarily through optical emission and moderate X-rays, while in LMXBTs they dominate the high-energy part of the spectrum. However, it is the outbursts and their behaviour that highlight the most important resemblance between these families. Evidently an identical, or at the least a similar, underlying mechanism must be present in both systems.

1.3 Outbursts in Accreting Binary Systems

Outbursts observed in accreting close binary systems are widely believed to be driven by the same underlying physical mechanism: disc instability. The disc instability model (DIM) was first proposed by Osaki (1974) to explain the recurrent eruptions of dwarf novae. In its original form, the model was based on a thermal–viscous instability in a geometrically thin accretion disc, assuming a constant mass-transfer rate from the donor star. Under these assumptions, the disc undergoes cyclic transitions between a cool, low-viscosity state and a hot, high-viscosity state, giving rise to periodic increases in luminosity.

Subsequent observational and theoretical developments demonstrated that this simplified picture is incomplete. It is now understood that the mass-transfer rate from the donor

can vary on a wide range of timescales and that additional physical processes play an important role in shaping the outburst behaviour. In particular, irradiation of the accretion disc and donor star by high-energy radiation, tidal interactions within the binary, and heating associated with the impact of the mass-transfer stream can significantly modify the disc structure and its stability properties (e.g., Smak 2000; Lasota 2001).

The Disc Instability Model

The DIM explains outbursts as a consequence of a thermal and viscous instability operating in geometrically thin accretion discs. The instability arises from the strong temperature dependence of the disc opacity in the regime where hydrogen undergoes partial ionization. As the local disc temperature approaches this ionization threshold, small perturbations in temperature or surface density can lead to large changes in opacity and viscosity, destabilizing the disc (Lasota 2001; Frank et al. 2002).

This behaviour is commonly illustrated using the local thermal equilibrium solutions of the disc, expressed in terms of surface density Σ and effective temperature $T_{\rm eff}$ or mass accretion rate $\dot{M}$. For a given radius, these parameters form a theoretical S-shaped curve in the Σ–$T_{\rm eff}$ plane. The lower branch of the so called *S-curve* corresponds to a cool, neutral disc state, characterised by a low value of the viscosity parameter $\alpha_{\rm cold}$. The upper branch represents a hot, ionized, high-viscosity state given by $\alpha_{\rm hot}$. The intermediate branch is thermally unstable and cannot be achieved, as it impossible for the disc to raise its temperature by lowering its surface density when moving from the lower branch to the upper and vice-versa. As a result, the disc instead undergoes transitions between the two stable states.

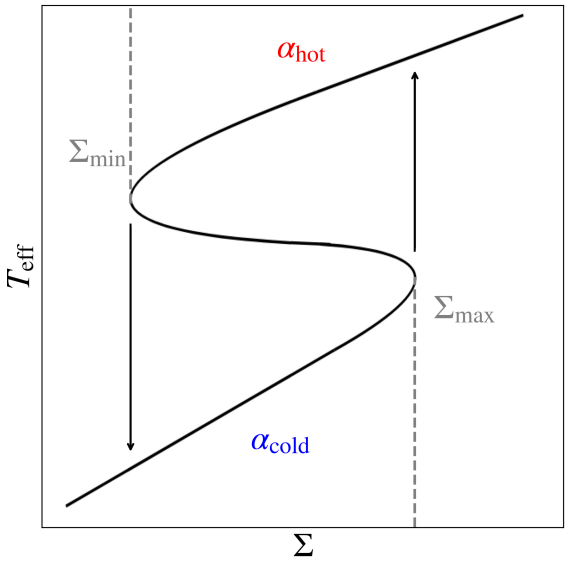

Figure 1.1: Schematic representation of the S-curve. See text for details.

We can illustrate such a transition by examining how the surface density Σ evolves as a function of disc radius R, as shown in Fig. 1.2. When the disc is in a cold state, it accumulates matter faster than it can transport it inward. Eventually, the surface density reaches the upper critical value $\Sigma_{\rm max}$ and therefore a critical temperature, resulting in hydrogen ionization which drastically changes the opacity and viscosity in this region. Such an extreme change triggers a heating front, propagating through the disc. In the lightcurve, this corresponds to a rapid rise to outburst, until the entire disc is hot and ionized, reaching its maximum luminosity. This process is captured in Fig. 1.2b, where typical Σ profiles show the heating front advancing outward through the disc. In the hot state, however, matter flows out of the disc faster than it flows in. When the surface density drops to the lower critical value $\Sigma_{\rm min}$, a cooling front is triggered, propagating throughout the disc. This is seen as the decline from maximum in the lightcurve until the entire disc returns to its initial cold state, observed as quiescence. The inward propagation of such a cooling front is shown in Fig. 1.2a.

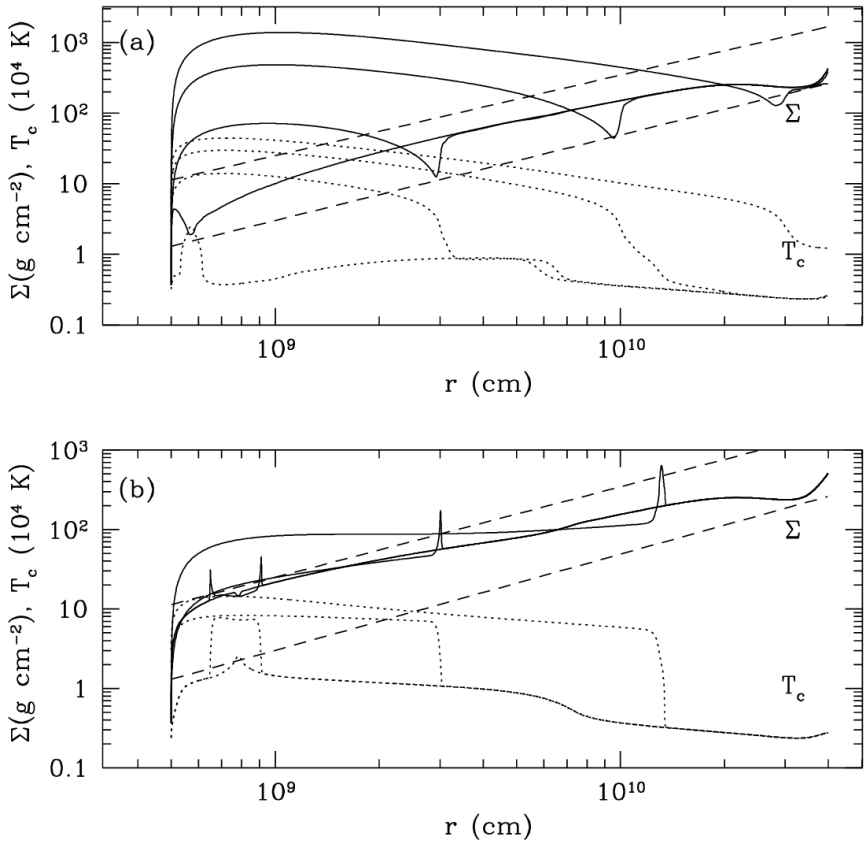

Figure 1.2: Typical evolution of the surface density Σ (solid lines) as a function of disc radius during the propagation of a cooling front (a) and an inside-out heating front (b). The dashed lines represent the critical surface densities $\Sigma_{\rm min}$ (upper curve), the minimum surface density of the hot branch, and $\Sigma_{\rm max}$ (lower curve), the maximum surface density of the cold branch. In panel (a), the cooling front propagates inward, returning the disc to the cold state as Σ drops below $\Sigma_{\rm max}$. In panel (b), the heating front propagates outward, bringing the disc into the hot state as Σ exceeds $\Sigma_{\rm min}$. Figure from Lasota (2001).

As we can see, the rate at which the disc receives matter is very important for outburst description. We can get a clearer picture by modifying Fig 1.2 and expressing the critical $\Sigma_{\max}$-curve in terms of the mass accretion rate $\dot{M}$. This way, we receive the instability limit curve of $\dot{M}_{\max}$, where an intersection of this curve will result in an outburst as described in the previous paragraph. In Fig. 1.3, beyond the outer disc edge are plotted possible mass-transfer rates from the secondary, which we can approximate as constant on timescales relating to outbursts. Three options arise:

- **Low mass-transfer rate systems** do not not connect with the instability limit curve, rarely ever exhibiting outbursts. They are in fact so dim, that their quiescence luminosity is even lower than the quiescence observed in systems with regular outbursts.
- **Intermediate mass-transfer rate systems** do intersect the instability limit curve, resulting in standard recurrent outbursts in their accretion discs, by which we characterize these systems as dwarf novae.
- **High mass-transfer rate systems** spend most of their lifetime in a luminous high state. Their stable hot accretion disc may plateau due to fluctuations in the mass-transfer rate, but no cyclic outbursts are observed. Such systems are called nova-likes.

As an added benefit, we can now schematically see why disc truncation also plays a large role in outburst behaviour. Specifically, why we may observe stable discs in intermediate mass-transfer rate systems. Here, the instability limit curve should be intersected and result in observed outbursts. However, if this curve was shorter, i.e., if it would not extend all the way down to the white dwarf surface, no intersection would happen, resulting in stable discs like those in low mass-transfer rate systems. The curve would instead extend only to the magnetospheric radius in magnetic systems (intermediate polar CVs), or to a radial distance determined by evaporation in highly-radiative systems (LMXBTs) (see Warner 1995; Lasota 2001).

1.4 Dwarf Novae

Dwarf novae are characterised by recurrent outbursts during which their optical brightness increases by several magnitudes. These regular outbursts also have varying shape, either narrow and comparably more symmetrical or wide with a slower decay. Apart from these normal outbursts, some dwarf novae can exhibit superoutbursts: much longer and brighter events. These occur when the disc expands beyond the 3:1 resonance radius, causing tidal deformation and disc precession. This leads to enhanced mass transfer that results in a more luminous and prolonged outburst, characterised by a superhump in the lightcurve (Osaki & Kato 2014). Superoutbursts are usually separated by many normal outbursts. Their *recurrence time* (the interval between successive outbursts) is therefore much longer.

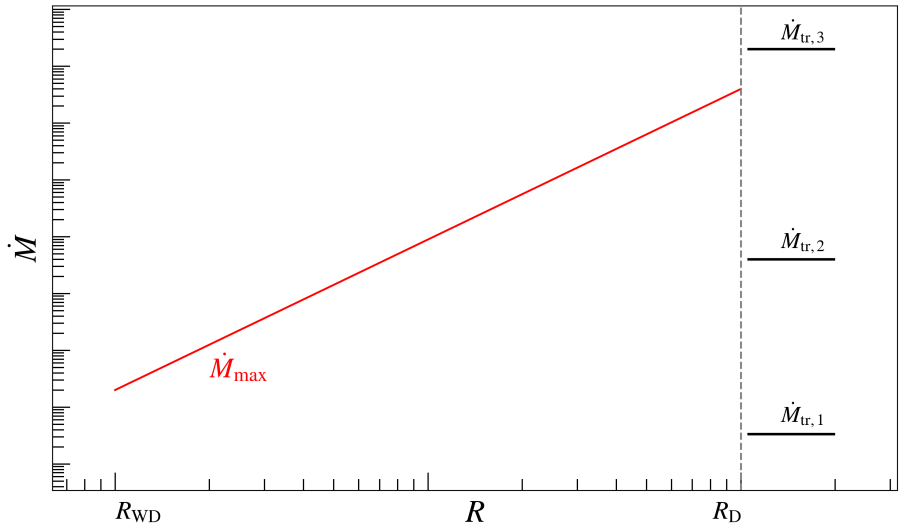

Figure 1.3: A schematic instability limit curve. Low, intermediate and high mass-transfer rates from the secondary are plotted as $\dot{M}_{\mathrm{tr,\,1}}$, $\dot{M}_{\mathrm{tr,\,2}}$ and $\dot{M}_{\mathrm{tr,\,3}}$ respectively. Details of the $\dot{M}_{\mathrm{max}}$-curve can be found in equation (A.2) in Lasota (2001).

According to their outburst behaviour, dwarf novae can be further divided into three principal subclasses: U Gem-type, SU UMa-type, and Z Cam-type systems, named after their prototypes. Their defining characteristics can be summarized as follows:

- **U Gem-type systems** exhibit only normal outbursts with relatively regular recurrence times.
- **SU UMa-type systems** show both normal outbursts and superoutbursts. In some extreme cases, known as WZ Sge-type systems, only superoutbursts are observed, separated by very long quiescent intervals.
- **Z Cam-type systems** are distinguished by the presence of standstills, intervals during which the system remains at an intermediate brightness level, slightly below the outburst maximum. These standstills can persist from weeks to several years and are thought to occur when the mass-transfer rate temporarily approaches the critical value separating stable and unstable disc states.

What also reflects the division of CVs as a consequence of the DIM is their observed period distribution, seen in Fig. 1.5. Systems below the period gap have lower mass-transfer rates, unable to reach the critical value for stability. Therefore, the short-period population of CVs are practically dominated by dwarf novae. Above the gap, however, dwarf novae and nova-likes exist almost equally within the population. This observed coexistence may be attributed to mass-transfer-rate fluctuations on unobservably large timescales (Knigge et al. 2011).

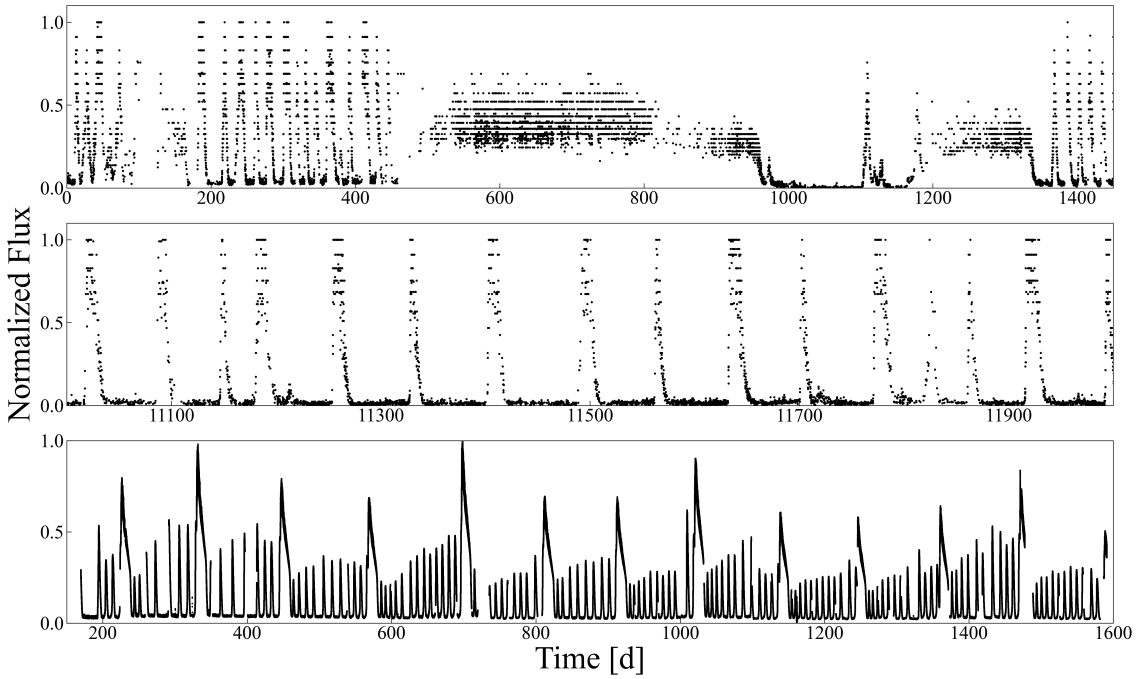

Figure 1.4: *Top:* the light curve of Z Cam-type dwarf nova RX And. Data from AAVSO. *Middle:* the light curve of U Gem-type dwarf nova SS Cyg. Data from AAVSO. *Bottom:* the light curve of SU UMa-type dwarf nova V344 Lyr. Data from MAST.

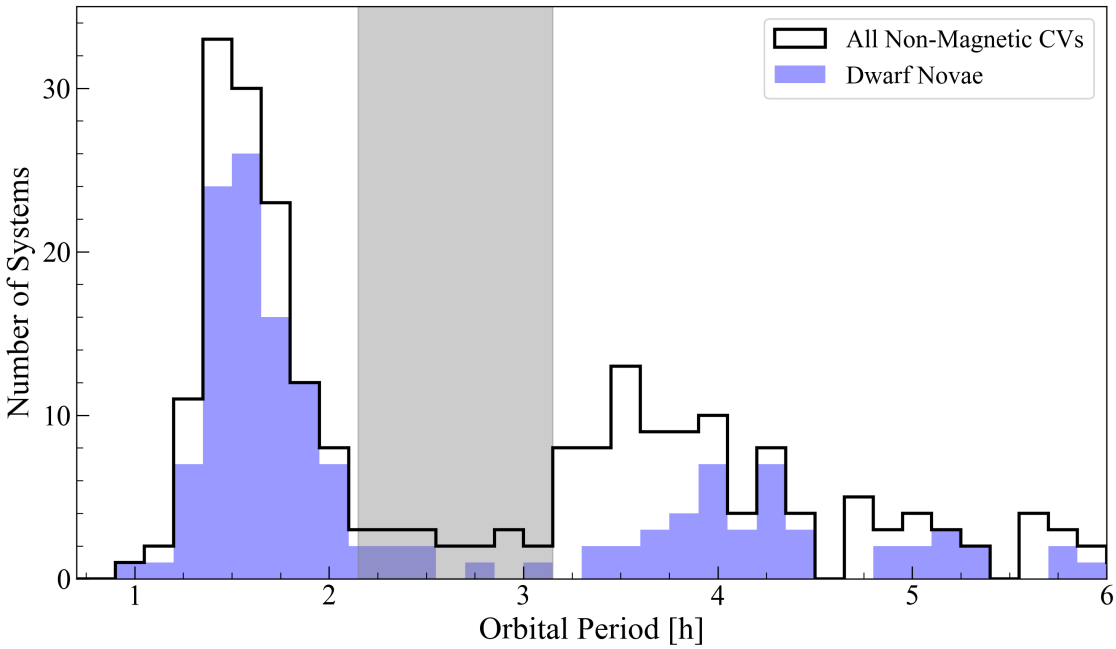

Figure 1.5: The orbital period distribution of non-magnetic CVs in the CVCAT catalog (Downes et al. 2001). The blue shaded area represents the dwarf nova population and the gray shaded area shows the period gap (see Knigge et al. 2011 for exact value).

Inside-Out and Outside-In Outbursts

Dwarf nova outbursts can be classified according to the radial location at which the thermal instability is first triggered and the direction in which the resulting heating front propagates. These are commonly referred to as inside-out and outside-in outbursts (Lasota 2001).

The main factor determining the outburst type is the mass-transfer rate from the donor star compared to the viscous diffusion timescale of the accretion disc. At relatively high mass-transfer rates, matter accumulates near the outer edge of the disc. If the accumulation timescale there is shorter than the timescale on which viscosity can redistribute the material inward, the critical surface density $\Sigma_{\rm max}$ is first exceeded at large radii, triggering an outside-in outburst. On the other hand, at lower mass-transfer rates, material has sufficient time to diffuse inward and accumulates in the inner disc regions, where viscous evolution is faster. In this case, the instability is initiated near the white dwarf, producing an inside-out outburst (Lasota 2001).

The subsequent propagation of the heating front differs significantly between the two cases. Outside-in fronts travel inward along the surface-density gradient and propagate efficiently, rapidly bringing a large fraction of the disc into the hot, ionized state. Inside-out fronts, however, must propagate outward against the surface-density gradient. This requires substantial angular momentum transport and mass redistribution. If the surface density behind the front is insufficient, the front may stall and be reflected as a cooling front, preventing the disc from fully entering the hot state. Outside-in outbursts are therefore commonly associated with fast-rise, asymmetric light curves, while inside-out outbursts tend to exhibit slower, more symmetric profiles. It is also important to note, that even though heating fronts can be of both the outside-in and inside-out type, cooling fronts which return the disc to its cold state can only be of the outside-in type. This is because after an outburst, the lower critical surface density $\Sigma_{\rm min}$ is always reached at the outer, emptied disc edge.

The UV Delay

An important observational consequence of the structure of dwarf nova outbursts is the so-called UV delay, defined as the time lag between the rise of the optical flux and the subsequent increase in ultraviolet (UV) or extreme ultraviolet (EUV) emission. The existence of this delay is a natural outcome of the separation between the regions dominating the optical and high-energy emission.

The optical emission is produced predominantly by the cooler, extended outer disc, whereas the UV and EUV emission originates mainly in the hot inner disc and the boundary layer close to the white dwarf. In outside-in outbursts, the outer disc heats up first, leading to an immediate rise in optical brightness. The UV emission increases only once the heating front reaches the inner disc, producing a delay of order hours to days. In inside-out outbursts, although the instability begins near the white dwarf, the initially heated region is small and the accretion rate remains low. As a result, the optical flux rises only after the heating front has propagated outward, and a UV delay is still generally expected as a result of the model. However, simulations show that the UV delay cannot be used as a reliable indicator of the outburst type. Schreiber et al. (2003) demonstrated that the UV delay at the start of an outburst can be longer for inside-out outbursts than for outside-in

ones. This is mainly because inside-out heating fronts propagate against surface-density gradients, slowing the rise of the central accretion rate, whereas outside-in fronts travel with the gradient. These findings come from simulations that include disc truncation as the primary mechanism, along with additional effects such as heating by stream impact and a variable outer disc radius (Smak 1998; Schreiber et al. 2003)

Low-Mass X-ray Binary Transients

We know that the outbursts in both CVs and LMXBTs are believed to be driven by the same thermal-viscous processes operating in the disc. However, the application of the DIM to LMXBTs requires important modifications due to the high-energy environment associated with accretion onto neutron stars and black holes.

The most significant difference compared to CVs is the role of X-ray irradiation. In LMXBTs, intense X-ray emission from the inner accretion flow irradiates the outer disc, strongly influencing its thermal structure and stability. Irradiation keeps the outer disc in the hot state for longer than in the standard DIM, which explains the longer outburst durations observed in LMXBTs compared to dwarf novae. The outburst decline in this case is not driven by the propagation of a cooling front as in the standard model, but by the gradual decrease of the mass accretion rate and consequently the irradiating flux, which eventually becomes too weak to sustain the hot state. As a consequence, the optical emission observed during LMXBT outbursts is largely produced by reprocessing of X-rays in the outer disc rather than by local viscous dissipation. The failure of simple models based on point-source irradiation to illuminate a geometrically thin disc implies the presence of extended scattering regions, warped discs, or coronae (Lasota 2001).

In addition to irradiation, disc truncation is thought to be essential for explaining the long recurrence times and quiescent behaviour of LMXBTs. In quiescence, the inner disc is likely replaced by a hot, radiatively inefficient flow, while during outburst the disc refills and extends inward. Within this truncated and irradiated model, many observed properties of LMXBTs, such as fast-rise exponential-decay outbursts, long recurrence times, and delays between optical and X-ray emission can be reproduced.

We have so far focused on the long-term phenomena of accreting binary systems, particularly the long-term variability and outbursts driven by disc instabilities. However, accretion flows also exhibit pronounced variability on much shorter timescales, arising from local and dynamical processes that cannot be captured by global disc evolution alone.

1.5 Flickering

Flickering refers to the rapid, aperiodic brightness variations observed in accreting systems. It occurs on timescales from seconds to tens of minutes and is detectable across wavelength range from optical to X-rays. Observationally, flickering is characterised by stochastic, “red-noise” variability in the light curve, with power decreasing toward higher frequencies. This phenomenon is found in CVs, LMXBTs and active galactic nuclei, suggesting a universal origin connected to the accretion process.

Flickering variability is usually analysed through the *power density spectrum* (PDS), which represents how the variability power is distributed over frequencies. By examining the characteristics of this variability, we can see that flickering has three fundamental properties:

1. **rms-flux relation.** The variability amplitude, taken as the root-mean-square (rms) of the flux, is found to scale linearly with the mean flux. This relation has been observed in CVs such as MV Lyrae and V1504 Cyg (e.g., Scaringi 2014; Dobrotka et al. 2016). The linearity implies that flickering is a multiplicative process, where fluctuations generated at different disc radii combine together, rather than being independent additive events.

2. **PDS and characteristic frequencies.** Flickering produces a red-noise PDS, which forms the broad-band baseline. Stacked on this baseline are individual Lorentzian components or breaks in the power-law slope, each associated with a characteristic frequency. In CVs, these break frequencies are generally found at much lower values than in LMXBTs, reflecting the larger size and longer characteristic timescales of white dwarf accretion discs. For example, the nova-like MV Lyrae exhibits several characteristic breaks around $\log(f/\mathrm{Hz}) \sim -3.0$ to -1.6 (Scaringi 2014), while dwarf novae show a low-frequency break near $\log(f/\mathrm{Hz}) \sim -3.4$ in quiescence, with additional high-frequency components appearing during outburst. It is however important to state that the quiescent characteristic frequency does not disappear during outburst. Evidence therefore suggests that these frequencies are not tied to the specific flux, but rather the state of the disc as a whole (Dobrotka et al. 2016).

3. **Wavelength-dependent time lags.** Flickering variability is not simultaneous across all wavelengths: flares tend to peak slightly earlier at shorter (blue) wavelengths than at longer (red) ones. This behaviour suggests that the variability originates in the inner disc regions and propagates outward, or that higher-energy emission is produced closer to the compact object and is reprocessed by the cooler outer disc. These time lags provide strong evidence that flickering is connected to radial propagation processes in the accretion flow (Scaringi 2014).

Propagating Accretion Rate Fluctuations

The most successful physical interpretation of flickering is the model of propagating mass accretion rate fluctuations (Lyubarskii 1997; Kotov et al. 2001; Arévalo & Uttley 2006), which we will simply refer to as the fluctuating accretion disc model. In this description, accretion flow is not steady, but exhibits stochastic variations in the local mass accretion rate at each disc radius. These fluctuations occur on the local viscous timescale and propagate inward, combining multiplicatively with fluctuations generated at smaller radii. As a result, the variability observed near the white dwarf is the product of fluctuations generated throughout the disc, producing the observed broad-band noise. This multiplicative nature explains the linear rms–flux relation. Additionally, application of the model to MV Lyrae suggests that the inner accretion flow is geometrically thick, resembling a corona-like structure, and extends to large radii, implying that the standard thin disc is insufficient to explain the high-frequency variability (Scaringi 2014). In dwarf

novae, the characteristic flickering frequencies change between quiescence and outburst: during quiescence the inner disc is likely truncated into a hot corona with a geometrically thick flow (also referred to as an advection-dominated accretion flow, or ADAF, Narayan & Yi 1995), producing only low-frequency variability, while during outburst the inner disc reforms, generating additional high-frequency components (Dobrotka et al. 2016). The enhanced turbulence in the inner regions during outburst may arise from Kelvin–Helmholtz instabilities between the thin disc and the hot flow, and the observed optical flickering may be produced by X-ray reprocessing in the thin disc.

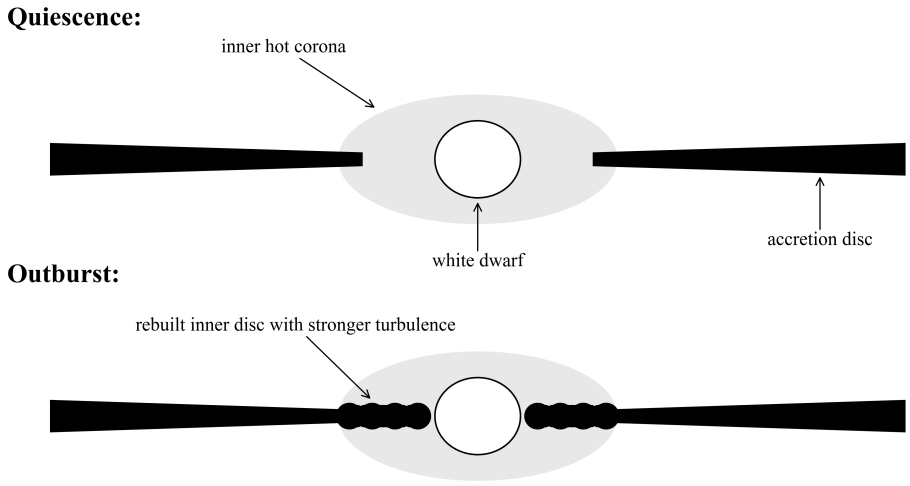

Figure 1.6: A possible model explaining the origin of characteristic frequencies during dwarf nova quiescence and outbursts. See text for details.

Chapter 2

V1504 Cyg Analysis

2.1 Data

The analysis presented in this work is based on high-cadence optical photometry obtained by the NASA *Kepler* mission (Borucki et al. 2010). The spacecraft, launched in March 2009, was designed to monitor a fixed 115-square-degree field of view in the constellations Cygnus and Lyra. It utilized a 0.95-meter Schmidt telescope feeding a photometer composed of an array of 42 CCDs, operating with a broad spectral range from approximately 400 to 850 nm. By avoiding the interruptions of ground-based observatories, *Kepler* provided quasi-continuous monitoring with exceptional photometric precision, making it an ideal instrument for characterizing fast stochastic variability such as flickering.

The observations were, however, not strictly uninterrupted. The spacecraft was required to perform quarterly rolls to maintain proper orientation of its solar arrays, and regular data downlinks for monthly re-pointings. Furthermore, the spacecraft occasionally entered unexpected safe modes triggered by hardware anomalies or cosmic ray events. These operational constraints resulted in specific data gaps within the lightcurves. The handling of these gaps is detailed in subsequent sections, as their impact on the analysis and their required mitigation differs between the PDS and AFP methods. This distinction highlights a specific advantage of the flare profile approach and validates its inclusion in this study.

The specific target of this study, V1504 Cyg (KIC 7446357), is an SU UMa-type dwarf nova with an orbital period of $P_{\mathrm{orb}} \approx 1.67\,\mathrm{h}$. The system was observed by *Kepler* in 58.8 s Short Cadence (SC) mode. We retrieved the photometry from the Mikulski Archive for Space Telescopes (MAST)[1]. The resulting lightcurve spans approximately 1400 days, exhibiting 118 normal outbursts separated by quiescent intervals. These outbursts are organized into supercycles, which are segments of the lightcurve bounded by subsequent superoutbursts. In total, the dataset covers 13 supercycles, fully containing 12 distinct superoutbursts within the observational window. The full lightcurve can be seen in Fig. 2.1.

To make sure the analysis focused on our specified goal, we applied strict selection criteria to the lightcurve segments. First, all superoutbursts were excluded from the dataset for a simple reason. The much stronger amplitude of superoutbursts compared to

[1]The described data may be obtained from https://dx.doi.org/10.17909/T90K5C

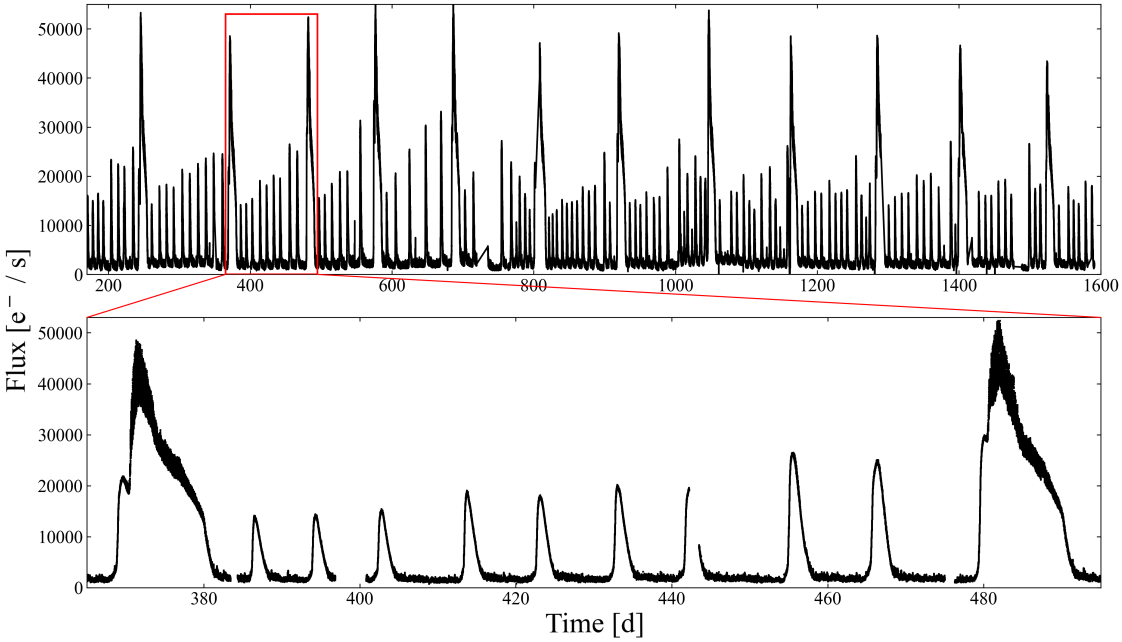

Figure 2.1: The entire *Kepler* lightcurve of V1504 Cyg, including a zoomed-in typical supercycle.

outbursts suggests an additional, more extreme physical process being present. Apart from superhump activity also being evidence for another physical mechanism, it also drastically changes the shape of superoutbursts in the lightcurve. Such a different profile would require a modified approach when compared to regular outbursts. Therefore, we restricted our analysis strictly to these and their subsequent transition to quiescence.

On top of that, not all of the 118 normal outbursts were suitable for study. A critical requirement for outburst identification and analysis is the presence of the outburst maximum, which serves as the main reference point for every outburst. In several cases, data gaps occurred close to the peak of an outburst, making the determination of the exact maximum impossible. These incomplete outbursts were removed from the sample. We retained the surrounding quiescent data as to not interfere with neighboring, valid outbursts.

This way, we removed a total of 12 superoutbursts and 4 potential outbursts with missing data near the maximum. The specific excluded time ranges are listed in Table 2.1.

Outburst Identification

With the dataset prepared, we proceeded to identifying the individual normal outbursts suitable for our analysis. The identification process was performed in two stages: an initial search to locate significant peaks, followed by a refinement step to precisely define the outburst maximum.

First, we performed a rough search for peaks in the lightcurve using the `find_peaks` function from the `SciPy` signal processing library (Virtanen et al. 2020). We imposed a `prominence` threshold of 10 000 flux counts. This parameter effectively measures how much a peak stands out from the surrounding baseline of the signal. By setting the

Table 2.1: Time intervals excluded from the analysis due to the presence of superoutbursts (SO) or data gaps obscuring the normal outburst maximum (Gap).

Start Time [d]	End Time [d]	Reason
241	260	SO
368	382	SO
441	446	Gap
478	494	SO
572	590	SO
682	700	SO
800	820	SO
916	932	SO
968	972	Gap
1045	1058	SO
1160	1176	SO
1272	1278	Gap
1280	1298	SO
1370	1376	Gap
1394	1420	SO
1521	1538	SO

prominence to this level, we ensured that only significant outbursts, those with a flux count sufficiently distinct from the local background, were detected.

This prominence threshold also served as an implicit filter against outbursts separated by very short quiescent intervals. In such cases, the system does not return to a stable baseline before the onset of the subsequent outburst, resulting in a lower calculated prominence. Excluding these events was essential for maintaining consistency in our analysis. If we were to include outbursts with short quiescence, the analysis window would eventually overlap with the rising part of the following outburst. Avoiding this overlap would require shortening the analysis duration for specific events, thereby introducing variable criteria across the sample. By rejecting these low-prominence events, we ensured that all analysed outbursts were followed by a sufficiently long quiescent period. Excluding these outbursts together with 4 others exhibiting a data gap near their maximum mentioned earlier, we are left with 112 valid, regular outbursts ready for our analysis.

Lastly, these approximate peaks had to be refined, as to ensure we identified the true maximum which is symmetric about the outburst cap. Small perturbations in the flux may have caused our initial peaks to be offset. Therefore, we applied Locally Weighted Scatterplot Smoothing (LOWESS) using the `statsmodels` library (Seabold & Perktold 2010) to a narrow window of ± 0.15 d centered on each roughly identified peak. We utilized a smoothing fraction of `frac = 0.1`, meaning 10% of the data points within the window were used to calculate the local regression. An exmaple of a smoothed outburst cap can be seen in Fig. 2.2. The maximum value of this smoothed profile was then adopted as the definitive outburst maximum, serving as the reference point for all subsequent analysis.

Outburst Binning

The next step to prepare our outbursts for analysis was to divide their lightcurve into a series of discrete time segments (Bins). The definition of the Bin width Δt required a careful balance between resolution and statistical robustness.

In the context of PDS analysis, the Bin duration dictates the fundamental frequency resolution and the lowest detectable frequency ($f_{\min} \approx 1/\Delta t$). Ideally, a longer Bin duration is preferred to maximize the amount of photometric data available, thereby improving the signal-to-noise ratio of the resulting PDS. The same can be said for AFP analysis. The wider the Bin, the more flares can fit inside and be used for averaging, resulting in smaller errors. However, the physical properties of the accretion disc change rapidly during the outburst decay. If the Bins are too long, the characteristic frequency would evolve significantly *within* a single Bin, blurring the evolutionary trend we aim to resolve. On the other hand, if the Bins are too short, very little information can be extracted from either method.

This trade-off is partially mitigated by the size of our dataset. Since we analyze a collection of 112 outbursts, we can rely on averaging results across the same Bin from all outbursts to reduce noise, allowing us to utilize a shorter Bin width than would be possible for a single event.

Another critical constraint was the shape of the outburst rise. The transition from quiescence to outburst maximum is extremely steep. Attempting to analyze flickering variability during this fast rise is very problematic, as the strong trend dominates over any other variability. Therefore, we restricted our analysis to only the outburst cap and the subsequent decay. We placed exactly one Bin prior to the outburst maximum to ensure the Bin boundary did not extend into the steep rising phase.

Taking these factors into account, we adopted a uniform Bin width of $\Delta t = 0.25$ d. This duration balances the need for frequency resolution with the ability to trace the detailed evolution of the decay. The binning grid is referenced to the maximum of each outburst ($t_{\max}$). We defined 19 Bins in total:

- **Pre-maximum:** 1 Bin (Bin 0) covering the interval $[t_{\max} - 0.25\,d;\, t_{\max}]$.
- **Post-maximum:** 18 Bins (Bins 1–18) covering the interval $[t_{\max};\, t_{\max} + 4.5\,d]$.

This results in a total analysis window of 4.75 days per outburst. As described in the previous section, our selection criteria ensured that all analysed outbursts are followed by sufficient quiescence, preventing the final Bins (near $t_{\max} + 4.5$ d) from overlapping with the rise of a subsequent outburst. A visual representation of this binning scheme applied to a typical outburst is shown in Fig. 2.2.

Detrending

Our final step in the data preparation involved removing the underlying outburst decay trend from each Bin. This detrending is a fundamental prerequisite to analyse variability for both of our methods.

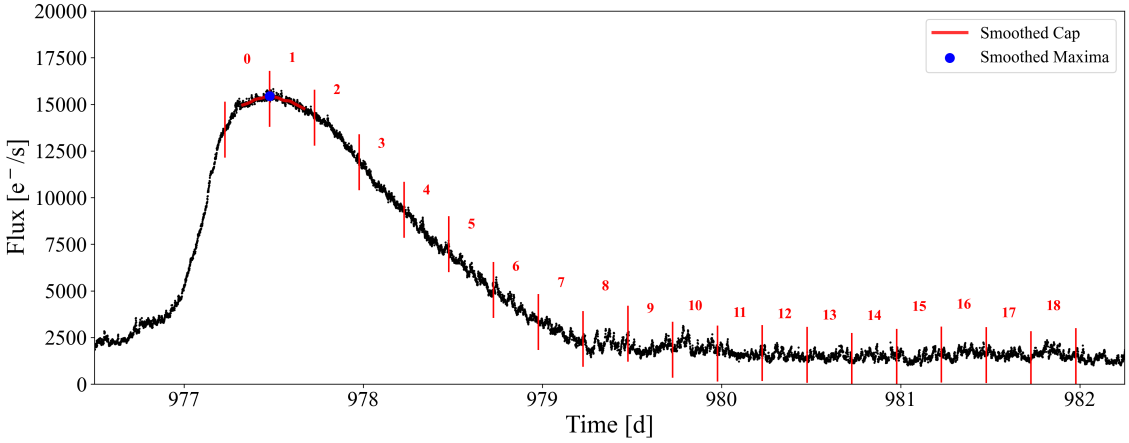

Figure 2.2: A typical outburst illustrating the binning scheme and a smoothed cap region. The vertical red lines indicate the Bin edges, with indexes above the centre of each Bin.

For any form of PDS analysis, the presence of a strong, non-periodic trend such as the steep, exponential decay of an outburst introduces significant power at the lowest frequencies. This "red noise" component dominates the spectrum and, due to spectral leakage, can obscure the flickering at higher frequencies (e.g., Deeter & Boynton 1982; Vaughan et al. 2003). Furthermore, reliable frequency analysis generally assumes the signal is locally quasi-stationary, meaning its statistical properties (such as mean flux) do not change drastically over the analysis window (Uttley et al. 2002).

Similarly, for the AFP method, detrending is essential to prevent geometric distortion of flare profiles. If individual flares were superimposed while riding on a steep slope, the resulting average profile would be tilted, skewing the symmetry of the shots and complicating the measurement of their characteristic timescales.

To address this, we applied a polynomial detrending algorithm to every outburst in our sample. The procedure was performed as follows:

- **Decay Phase (Bins 2–18):** The evolution of the flux in the later stages of the outburst is monotonic and relatively smooth. We fitted each of these Bins individually with a first-degree polynomial. This linear trend was then subtracted from the raw flux data of the corresponding Bin.

- **Outburst Cap (Bins 0–1):** The region surrounding the maximum is characterised by a curvature that a simple linear fit cannot capture. To accurately remove the bulk trend, we fitted Bins 0 and 1 together with a second-degree polynomial. This parabolic model was then subtracted from the data in these two Bins.

Subtracting the trend naturally shifts the mean flux of the Bins to zero. While mathematically correct for further analysis, this results in a disjointed lightcurve. To fix this for consistency, we applied a constant flux offset to the entire detrended outburst. The offset was calculated as the mean flux of unbinned quiescent data immediately after Bin 18. This effectively anchors the detrended tail to the true quiescent level of the system, preserving the relative flux scale during the outburst transition.

2.2 Power Density Spectrum Analysis

Before computing the PDS, we applied an additional selection on top of the 112 valid outbursts identified in the previous section. Since our approach treats each corresponding Bin from different outbursts as subsamples of the same physical state, every outburst must contribute a full set of 19 Bins with no missing intervals. Out of the 112 outbursts, 92 satisfied this condition. A further requirement regards the duration of the individual Bins. Equal Bin lengths are necessary for a consistent PDS estimate (van der Klis 1989). While very small data gaps within a Bin may cause minor fluctuations in Bin duration, a gap large enough to considerably shorten a Bin renders it unsuitable. Upon inspection, one of the 92 outbursts contained a Bin with a duration comparable to 0.25 d, and was therefore excluded. This left us with 91 outbursts for the PDS analysis.

For each of the 19 Bins, we constructed a mean PDS using Bartlett's method (Bartlett 1948), where instead of dividing a single long lightcurve into subsamples, we used the corresponding Bin from each of the 91 outbursts as an individual subsample. The periodogram of each Bin was computed using the Lomb-Scargle algorithm (Scargle 1982), implemented via the `LombScargle` class from the `Astropy`[2] Python library, which is suited for unevenly sampled data such as observations affected by data gaps. Furthermore, the `Astropy` implementation of the algorithm automatically subtracts the mean flux of each Bin prior to computing the periodogram, which is a requirement of the algorithm. This is useful in our case, because our Bins were offset as mentioned in section 2.1. All periodograms were first transformed into log-log space, as averaging $\log(p)$ rather than p directly is recommended by Papadakis & Lawrence (1993) for obtaining reliable PDS estimates. The mean of these $\log(p)$ values within each PDS interval then represents the PDS estimate for that Bin.

Before fitting, we determined the frequency range over which the PDS could be meaningfully analysed. After examining the averaged PDS over a wide frequency range, we set two boundaries. At the low-frequency end, around $\log(f/\mathrm{Hz}) \approx -3.8$, a broad peak is present, showing an excess of power corresponding directly to the orbital period of V1504 Cyg ($P_{\mathrm{orb}} \approx 1.67\,\mathrm{h}$). This feature does not reflect flickering variability and had to be excluded. At the high-frequency end, the upper limit is set by the Nyquist frequency, defined as half of the sampling frequency. For the *Kepler* short-cadence mode with a sampling step of 58.8 s, this gives $f_{\mathrm{Nyq}} = 1/(2 \times 58.8\,\mathrm{s})$, corresponding to $\log(f/\mathrm{Hz}) \approx -2.07$. Above this frequency, the data cannot reliably represent the signal. We therefore restricted our analysis to the frequency range $-3.6 \leq \log(f/\mathrm{Hz}) \leq -2.1$, which can be seen in Fig. 2.3.

Within the analysis region, the PDS was rebinned using a constant frequency interval of $\log(f/\mathrm{Hz}) = 0.1$. The uncertainty assigned to each rebinned point was taken as the standard error of the mean of the $\log(p)$ values within that frequency interval. We display the PDS with $\log(f \times p)$ on the vertical axis, rather than $\log(p)$, as this allows us to see the individual variability components more clearly.

[2] Astropy Collaboration et al. (2013, 2018, 2022)

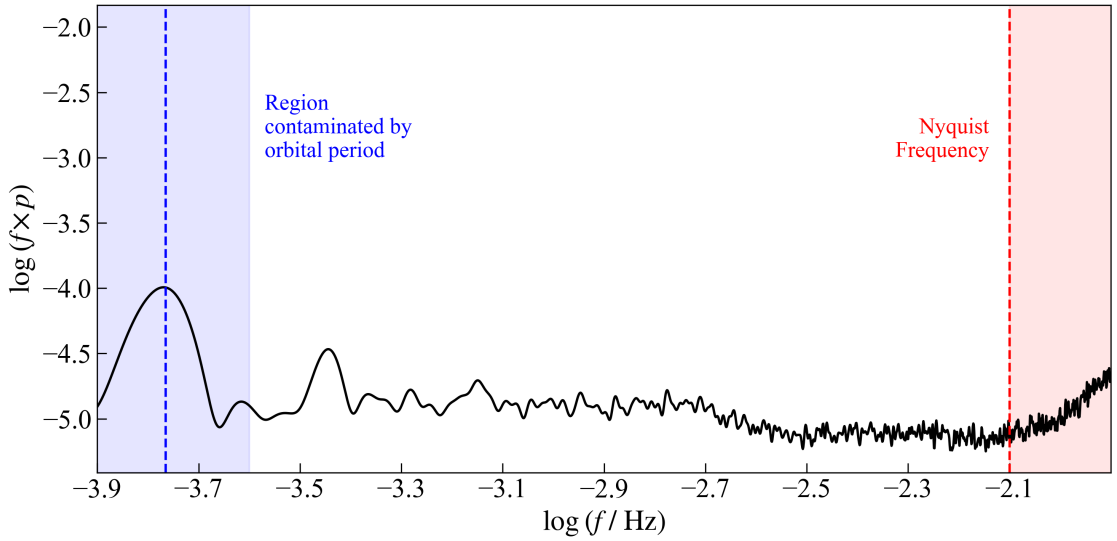

Figure 2.3: The averaged PDS of Bin 2 over a wide frequency range. The regions within and beyond the blue and red shaded areas are excluded from the analysis, corresponding to the orbital period of V1504 Cyg and the *Kepler* short-cadence sampling, respectively.

The rebinned PDS of each Bin was fitted with a broken power law model. Since we are working in log-log space, this is simply a piecewise linear function:

$$\log(f \times p) = A + s_i(\log f - \log f_{b,i}), \quad \log f_{b,i} \leq \log f < \log f_{b,i+1} \tag{2.1}$$

where A is the value of $\log(f \times p)$ at the first break frequency, s_i are the slopes of the individual power law segments, and $\log f_{b,i}$ are the break frequencies.

The number of breaks for each Bin was determined in two ways. In the first approach, it was established empirically based on the shape of the rebinned PDS. Bins 0–10 were described by two breaks, with the exception of Bin 6, which required only one. Bins 11–18, corresponding to quiescence, showed an additional high-frequency declining trend and therefore required three breaks. In the second approach, the number of breaks was determined by optimizing the reduced χ^2 of the model fit, defined as

$$\chi^2_\nu = \frac{1}{\nu} \sum_{i=1}^{n} \frac{(y_i - f_i)^2}{\sigma_i^2}, \tag{2.2}$$

where y_i are the observed data points, f_i are the corresponding model values, σ_i are the uncertainties, and $\nu = n - k$ is the number of degrees of freedom, with n being the number of data points and k the number of free parameters. The number of free parameters depends on the chosen model: a one-break model has $k = 4$, a two-break model has $k = 6$ and a three-break model has $k = 8$. A value of $\chi^2_\nu \approx 1$ indicates a good fit, while values significantly above or below unity suggest the model is respectively underfitting or overfitting the data. In correspondence with the empirical approach, three possible models were tested for each Bin (models with 1, 2 or 3 breaks), and the fit yielding the best χ^2_ν was selected. The results of both approaches and their comparison are presented in Chapter 3.

In both approaches, we focused exclusively on f_b, defined as the lowest break frequency of the fitted model. This is the frequency that falls within the interval of our interest, containing both the ~ 0.4 mHz quiescent component and the ~ 1 mHz outburst component, identified by Dobrotka et al. (2016). The evolution of f_b across the 19 Bins represents the main result of the PDS analysis.

2.3 Average Flare Profile Analysis

The PDS method, while powerful and greatly established, has two limitations in the context of this work. First, as seen in the previous section, it is sensitive to data gaps, requiring selection criteria that reduce the number of usable outbursts. Second, the PDS is a statistical description of variability in frequency space, and while it efficiently captures the overall power distribution, it does not directly reveal the morphology of the individual variability structures producing that power. The AFP method addresses both of these limitations and therefore serves as a natural complement to the PDS analysis.

The AFP method was first proposed by Negoro et al. (1994) for the analysis of *Ginga* data of Cygnus X-1. As demonstrated by the author, the structures identified in the AFP correspond directly to individual structures in the standard PDS. Furthermore, Dobrotka et al. (2019) showed that all structures detected in the AFP are also present in the auto-correlation function (ACF), which measures the similarity of a signal to a time-delayed version of itself. The ACF can reveal characteristic variability timescales without assumptions about variability shape. The AFP has an advantage over the ACF in its asymmetry, preserving information about whether a feature occurs before or after the flare peak. The PDS, being a broad statistical description, and the AFP, which directly visualizes individual variability structures, are therefore complementary rather than exclusive approaches.

The main idea behind the AFP method rests on the assumption that the accretion variability is driven by recurring physical processes. A feature forming and propagating through the accretion structure generates a characteristic flare profile. If the underlying accretion structure does not drastically change, repeated features produce flares with the same shape. A single flare is insufficient for analysis, as faint features are hidden in noise or blended with adjacent flares. By summing and averaging many individual flares, stochastic contaminations cancel out and only the coherent, physical structure remains. Because individual flare profiles are used regardless of whether the surrounding data is continuous, the AFP method is also robust against data gaps, provided the flare peak itself is not missing. This means all 112 valid outbursts established earlier could be used, compared to only 91 for the PDS analysis.

Flare Detection and Profile Construction

The construction of the AFP for each Bin has three main steps: flare identification, branch definition, and superimposition of the aligned flares. An additional correction step is applied at the end to account for a systematic bias introduced by Poisson noise.

Step 1: Flare identification Flares within each detrended Bin were identified using the same `find_peaks` function from the `SciPy` library used for outburst detection. Here, we

set the prominence to 300 flux counts, chosen empirically to exclude randomly deviated points caused by Poisson noise, while retaining only defined flares.

Poisson noise is an unavoidable source of uncertainty in any photometric measurement. A CCD, for example, individually counts arriving photons. This counting process is governed by Poisson statistics: if the true expected number of photons detected in a given exposure is N, the actual measured count will fluctuate around this value with a standard deviation of $\sigma_N = \sqrt{N}$. This means that brighter sources have larger absolute fluctuations but smaller relative ones, since the signal-to-noise ratio scales as $N/\sqrt{N} = \sqrt{N}$. In the context of flare detection, Poisson noise can cause individual data points to deviate significantly from the local mean flux, mimicking the appearance of a genuine flare peak. This introduces a systematic bias into the constructed flare profiles that must be accounted for. We describe how we addressed this effect at the end of this section.

Step 2: Branch definition Once a peak was identified, we assigned it a fixed extension of $N_{\text{ext}} = 25$ points on both sides, which we refer to as the rising and declining branches of the flare. This defined the full flare profile as a total of 51 points centered on the detected maximum. Given our cadence of 58.8 s, each branch spans approximately 1500 s, resulting in a total flare window of approximately 3000 s. To ensure that only isolated flares entered the analysis, we required that no two detected maxima were separated by fewer than N_{ext} points. If such an event occurred, both flares were discarded, preventing the declining branch of one flare from overlapping with the rising branch of the next and contaminating the averaged profile.

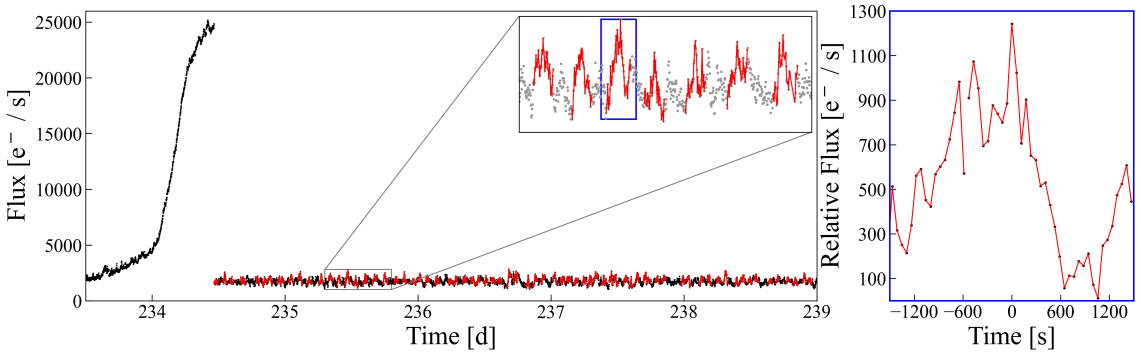

Figure 2.4: A detrended outburst, showing flickering within the inset. An example flare is shown in the right panel, defined by its peak and two branches. Detected flares are assigned an outburst index and a Bin index in which they were found.

Step 3: Superimposition To construct the AFP for a given Bin, all retained flares were aligned by their peaks and superimposed. The flux values at each point from the peak were then averaged across all contributing flares, and the uncertainty at each point was taken as the standard error of the mean of the contributing flux values. The mean minimum flux of the resulting profile was subsequently subtracted, placing the AFP baseline at zero.

Correction The central point of each AFP, corresponding to the detected flare peak itself, was excluded from all subsequent analysis. As described above, Poisson noise causes individual flux measurements to scatter around their true values. The peak-finding algorithm preferentially selects upward fluctuations, meaning the detected maximum is systematically biased toward higher flux values than the true flare peak. When many such biased peaks are stacked, the central point of the resulting AFP is artificially elevated, producing a central spike. This effect was studied in detail by Dobrotka et al. (2024), who showed that such a spike is additive and inconsistent with the observed variability properties. Therefore, we excluded the central point from all AFPs.

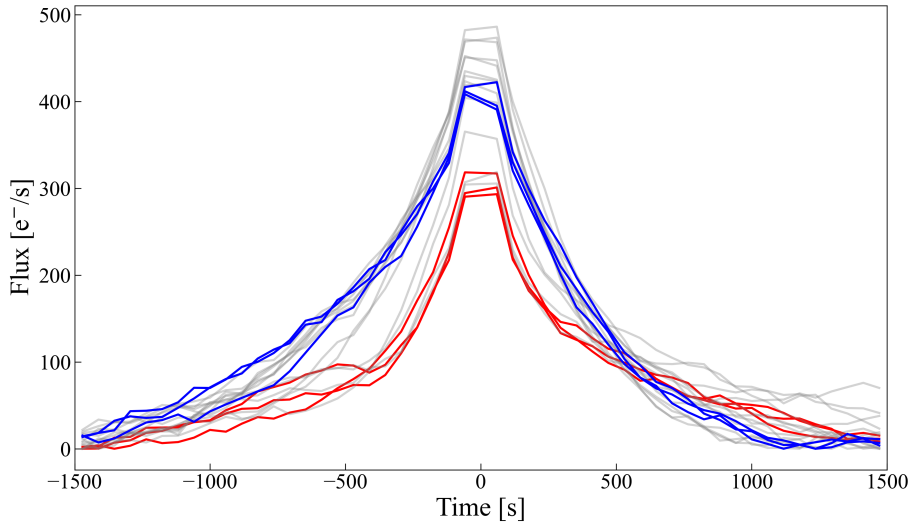

Figure 2.5: AFPs from all Bins with removed maxima compared together. The errors of the mean are not plotted. The first three Bins (with indexes 0, 1, 2) are plotted in red while the last three Bins (with indexes 16, 17, 18) are plotted in blue, while all other profiles are grey.

Flare Profile Fitting

With the 19 AFPs constructed, we proceeded to extract characteristic timescales from each profile. Inspecting the profiles, the overall shape of the flares is to a good measure approximated by an exponential rise followed by an exponential decline, motivating a model of the form:

$$\psi \sim e^{t/T_\mathrm{r}} \quad (t<0), \qquad \psi \sim e^{-t/T_\mathrm{d}} \quad (t>0), \tag{2.3}$$

where T_r and T_d are the rise and decline timescales respectively, and $t=0$ corresponds to the flare peak. Following Negoro et al. (2001), these timescales are directly related to characteristic frequencies in the PDS through $f_\mathrm{r,d} = 1/(2\pi T_\mathrm{r,d})$, allowing direct comparison with the break frequency f_b derived from the PDS analysis.

However, a closer inspection of the profiles reveals that the flare shape is not purely exponential. Both the rising and declining branches exhibit a linear trend at their outer edges, transitioning into the exponential closer to the peak. We therefore implemented three fitting methods of increasing objectivity and complexity, which we will describe now.

Method I: Empirical fitting range Motivated by Negoro et al. (1994), the AFP of each Bin was fitted with a piecewise exponential model,

$$\psi(t) = F_c + F_0 \begin{cases} e^{t/T_r} & t < 0 \\ e^{-t/T_d} & t \geq 0, \end{cases} \tag{2.4}$$

where F_c is the baseline flux and F_0 is the flare amplitude. The fitting range, taken as seconds from the peak on each side, was determined empirically: the range was extended until the fit departed outside the standard error of the mean of the AFP. This approach is straightforward but inherently subjective, as the fitting range depends on visual inspection.

Method II: Reduced χ^2_ν fitting range To remove the subjectivity of Method I, we retained the same piecewise exponential model, fitting both branches simultaneously, but determined the fitting range automatically. This time, the fitting range was defined as the number of points from the peak on each side. The minimal fitting range was chosen as 8 points from either side, the reason being that the number of free parameters in the fit is 4. All possible combinations of fitting range on the rising and declining sides were tested, and the combination yielding the best χ^2_ν was selected. This provides a more objective criterion for the fitting range and yields valid uncertainties on f_r and f_d.

Method III: Linear-exponential model The third approach accounts for the linear trends observed at the outer edges of the flare profile. The rising and declining branches are each fitted separately with a model consisting of a linear segment transitioning into an exponential at a free breakpoint,

$$\psi(t) = \begin{cases} a_r t + c_r & t < t_r \\ F_c + F_0\, e^{t/T_r} & t_r \leq t < 0 \\ F_c + F_0\, e^{-t/T_d} & 0 \leq t < t_d \\ a_d t + c_d & t \geq t_d, \end{cases} \tag{2.5}$$

where a_r and a_d are the slopes of the linear segments, t_r and t_d are the breakpoints between the linear and exponential regimes on the rising and declining branches respectively, and c_r, c_d are constants ensuring the model is continuous at the breakpoints. The breakpoints t_r and t_d are free parameters in the fit alongside T_r, T_d, a_r, a_d, F_c and F_0. The χ^2_ν of this fit is computed for each Bin. This model provides the most physically motivated description of the flare morphology and serves as the primary AFP result.

All fitting methods within the PDS and AFP analyses were implemented using the `curve_fit` function from `SciPy` (Virtanen et al. 2020). The uncertainties on f_b, T_r and T_d were obtained from the covariance matrix of each fit. Errors of T_r and T_d were subsequently propagated to f_r and f_d using the `ufloat` function from the `uncertainties`[3] Python library. The fitted profiles and the evolution of f_r and f_d across all 19 Bins are presented in Chapter 3.

[3] Available at: https://pythonhosted.org/uncertainties/

Chapter 3

Method Results

The fluctuating accretion disc model predicts that the characteristic frequencies of fast variability depend on the physical state of the accretion disc. Fluctuations in the mass accretion rate are generated throughout the disc and propagate inward on the local viscous timescale and combine multiplicatively. The observed variability therefore carries information about the entire disc. At the peak of an outburst, the disc is fully ionized and extends close to the white dwarf. As the system subsequently decays into quiescence, the inner disc retreats and the characteristic frequency is expected to decrease, because the variability timescale at a given radius scales with the local viscous timescale, which increases with distance from the central object. Which specific frequencies respond to these changes in the disc, and how, is the question this work aims to answer. The results presented in this chapter allow us to track the evolution of the flickering frequency across 19 outburst Bins. Additionally, by comparing the results of the PDS and AFP methods, as well as the individual fitting approaches within each method, we determine the consistency and robustness of our findings.

3.1 Power Density Spectrum

The PDS of all 19 outburst Bins, together with their broken power law fits, are shown in Fig. 3.1. In 15 out of 19 Bins, the empirical and χ^2_ν approaches agree on the number of breaks, and only a single fit in red is shown. In the remaining 4 Bins, the two approaches differ, and the empirical fit is additionally plotted in blue. The χ^2_ν value of each fit is displayed in the corresponding color in the upper right corner of each panel.

In the majority of cases for the red model, the χ^2_ν value is close to 1, confirming that the broken power law model provides an acceptable description of the PDS across all 19 outburst Bins.

The evolution of the break frequency f_b across all 19 Bins is shown in Fig. 3.2. The break frequencies derived from the χ^2_ν method are plotted in black for all Bins, while the four red points mark the Bins where the empirical approach yields a different number of breaks, plotted alongside for comparison. The red points do not deviate significantly from the black ones, in quiescence they agree almost perfectly, while the largest discrepancies

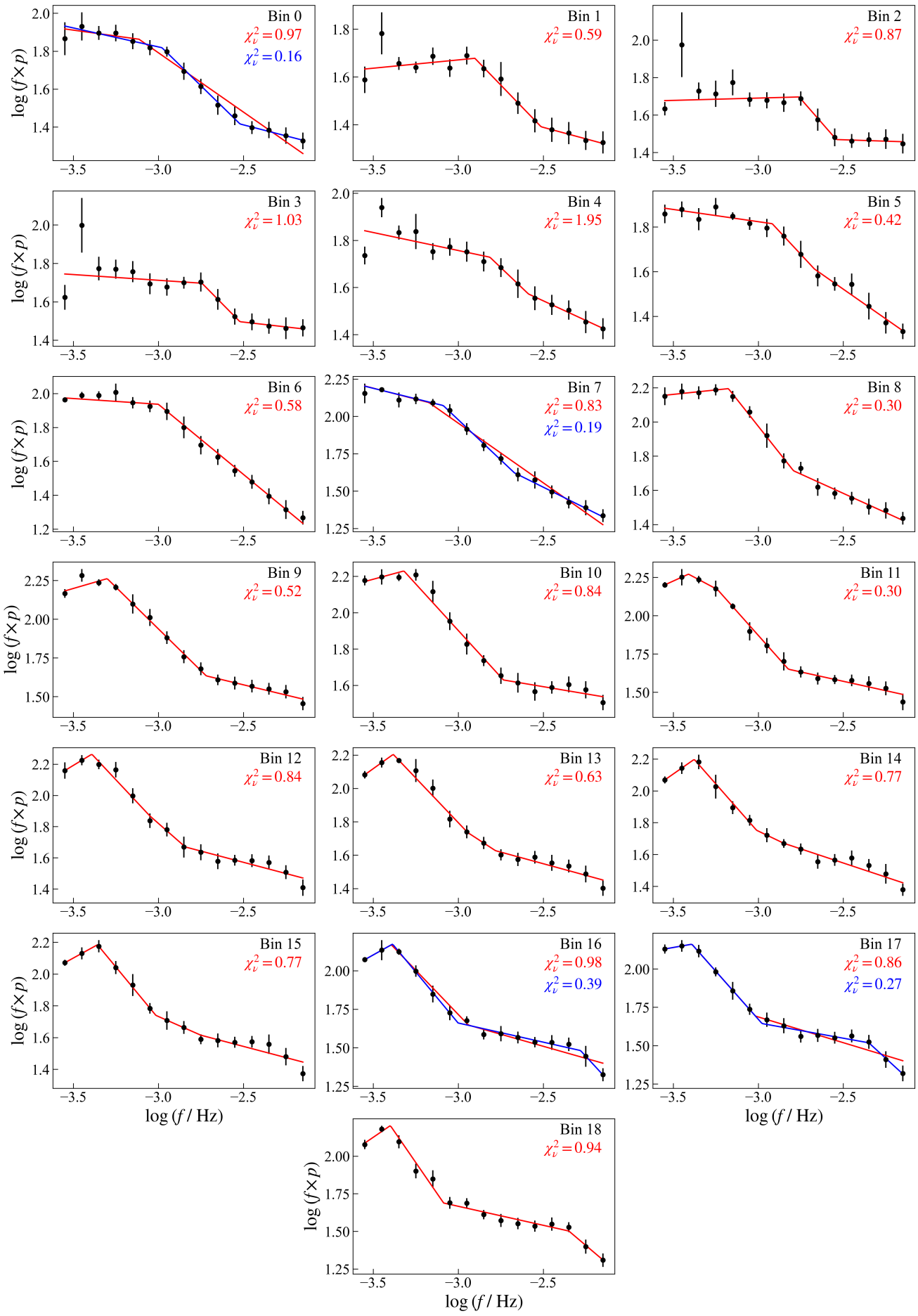

Figure 3.1: Broken power law fits of the PDS. Red fits represent the χ^2_ν method, while blue fits follow the empirical approach. If both methods agreed on the number of breaks, only the red fit is plotted.

occur earlier in the outburst, where the difference reaches at most $\Delta \log(f_b/\mathrm{Hz}) \approx 0.1$. This shows that the break frequency is robust against the choice of model complexity, and that the two approaches yield consistent results. For all subsequent analysis and comparison with the AFP method, we adopt the χ^2_ν results, as this approach is less subjective than the empirical one.

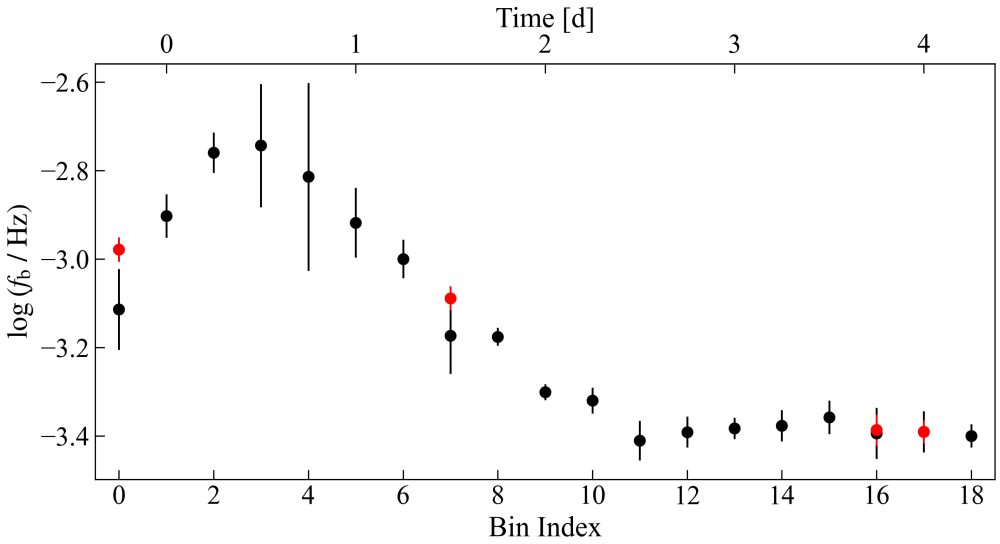

Figure 3.2: Evolution of the break frequency f_b across all 19 Bins of an outburst, gathered from the broken power law fits of the PDS. Red points represent fits with an empirical number of breaks in the model.

A dominant quiescent frequency of $\log(f_b/\mathrm{Hz}) \approx -3.4$ is clearly established after approximately 2 days following the outburst maximum, consistent with the value found by Dobrotka et al. (2016) for V1504 Cyg in quiescence. Another notable feature is that the break frequency does not reach its maximum at the outburst peak itself. Instead, it peaks around Bins 2–3, corresponding to approximately 0.5–0.75 days after the outburst maximum, before declining toward the quiescent value. It should be noted, however, that frequencies near the maximum are also among those with the largest uncertainties, so this observation should be treated with caution.

3.2 Average Flare Profile

The AFP method was applied together with the PDS not because the PDS is insufficient or more sensitive to data gaps, as it is already a well-established and robust tool, but for two specific reasons. First, the PDS frequency decline during the outburst decay is unambiguous, but the behaviour near the outburst maximum, where the frequency appears to peak after rather than at the maximum itself, relies on only a few Bins with large uncertainties. The AFP provides independent verification of this feature. Second, the AFP resolves the morphology of individual variability structures, which allows us to search for substructures such as the side-lobes identified by Dobrotka et al. (2019) in MV Lyr.

The resulting AFPs for all 19 Bins are shown in Fig. 2.5, and the individual fits of the profiles with our three models are presented in Fig. 3.4.

From Fig. 2.5, we can see a clear evolution in the flare shape as the outburst decays. The profiles in the first few Bins are the thinnest and have the lowest amplitudes. As the system evolves, the profiles begin to widen and their amplitude increases. The highest amplitudes are reached in the middle Bins, corresponding to the decline phase of the outburst, before dropping again as the system approaches quiescence.

We can also observe a change in functional shape, as in the early Bins, the profiles follow a clear linear-exponential trend. However, as the Bins progress toward quiescence, the linear part becomes less prominent and the profiles appear more purely exponential. Furthermore, the profiles are not entirely symmetrical, the two branches display different behaviour, especially in the early Bins. As the profiles become more exponential in the later stages of the outburst, the branches appear to become more symmetrical. Finally, we can see that no side-lobes like the ones detected by Dobrotka et al. (2019) in MV Lyr are present in any profile.

The evolution of the characteristic frequencies f_r and f_d across all 19 Bins is shown in Fig. 3.3, with the three methods plotted together for comparison. The top panel shows the rise frequency f_r and the bottom panel shows the decline frequency f_d. All three methods show the same overall trend: the frequencies are highest in the early outburst Bins, decline rather smoothly through the transition, and settle to a roughly constant value in quiescence.

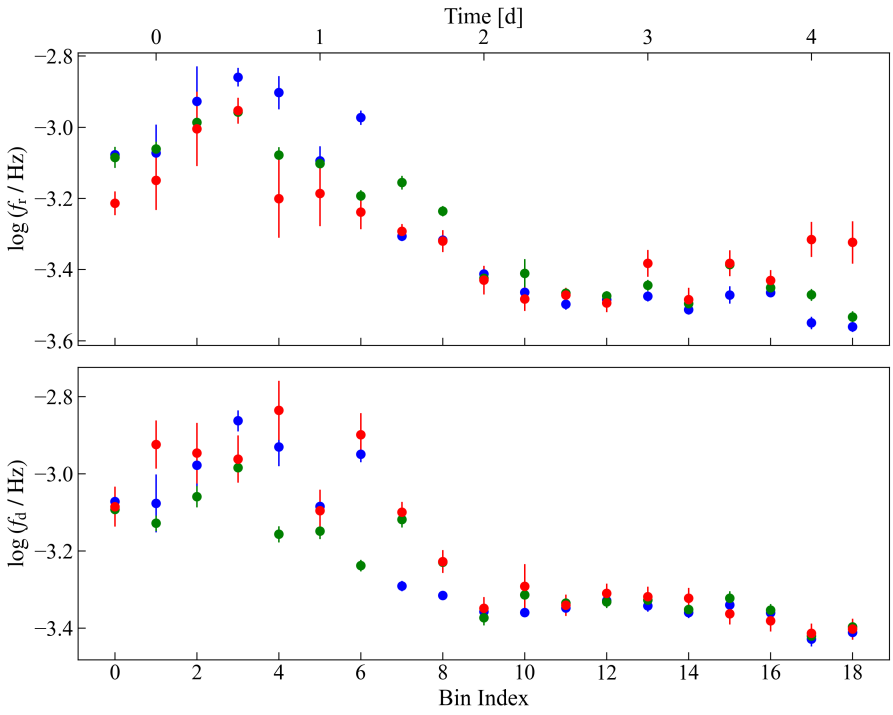

Figure 3.3: Evolution of the characteristic frequencies f_r (top) and f_d (bottom) across all 19 outburst Bins, derived from the AFP fits. Blue points correspond to Method I, green to Method II, and red to Method III.

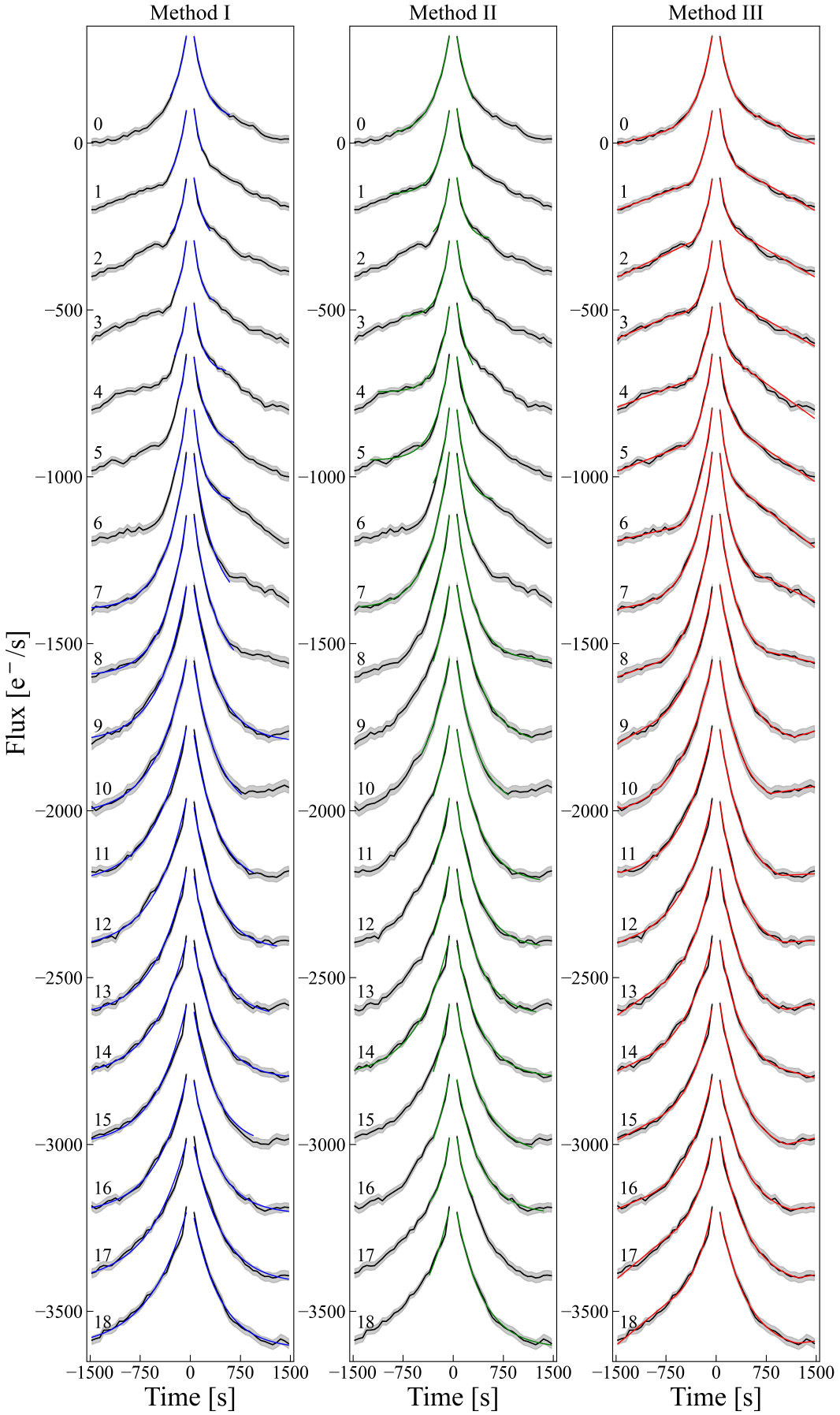

Figure 3.4: AFPs fitted with three models. Method I is shown in blue (left), Method II in green (middle), and Method III in red (right). The Bin index is indicated at the bottom left of each profile, which are offset by 200 flux counts for visual clarity.

For the rise frequency, Methods I and II (blue and green) yield consistently higher values than Method III (red) in the early Bins, while in quiescence all three methods converge. The decline frequency shows better agreement between the methods, especially in quiescence, although some scatter remains in the early Bins where the uncertainties are largest.

Despite the differences between methods, the behaviour is robust. In both f_r and f_d, the highest frequencies are reached around Bins 2–3, corresponding to approximately 0.5–0.75 d after the outburst maximum, with all methods peaking near $\log(f/\mathrm{Hz}) \approx -2.9$. The quiescent plateau is established by approximately Bin 9–10 (around 2–2.5 d after maximum) in both branches, settling near $\log(f/\mathrm{Hz}) \approx -3.4$. One notable feature of the frequency evolution is that while f_d settles into a stable quiescent plateau with small scatter, f_r exhibits noticeably more variability in the quiescent Bins.

As Method III provides the most physically motivated description of the flare morphology, we adopt its results as the primary AFP output. The numerical values of f_r and f_d from Method III, together with the PDS break frequencies, are summarized in Table 3.1. The χ^2_ν values for each fit and the number of contributing flares for the AFP are also listed.

Inspecting the χ^2_ν values in Table 3.1, the rise branch yields values closer to 1 on average than the decline branch, which tends to show lower values. This lower than 1 value indicates overfitting, meaning that the model has more flexibility than the data require. However, no branch shows systematically problematic fits. We conclude that linear-exponential model, while not perfect, can be considered a satisfactory description of the AFP shape across all Bins.

Table 3.1: Parameter results of fitting from the PDS χ^2_ν method and the AFP Method III.

	PDS		AFP				
Bin	f_b (mHz)	χ^2_ν	f_r (mHz)	χ^2_ν	f_d (mHz)	χ^2_ν	flares
0	0.769 ± 0.135	0.97	0.612 ± 0.039	0.15	0.823 ± 0.082	0.37	428
1	1.251 ± 0.118	0.59	0.709 ± 0.113	0.08	1.192 ± 0.143	0.54	451
2	1.739 ± 0.152	0.87	0.990 ± 0.199	0.55	1.132 ± 0.171	1.13	448
3	1.805 ± 0.482	1.03	1.113 ± 0.077	0.34	1.093 ± 0.129	0.65	466
4	1.534 ± 0.625	1.95	0.629 ± 0.132	0.63	1.461 ± 0.216	1.34	450
5	1.208 ± 0.182	0.42	0.652 ± 0.115	0.42	0.803 ± 0.084	0.84	459
6	1.000 ± 0.084	0.58	0.577 ± 0.053	0.24	1.263 ± 0.137	0.14	451
7	0.671 ± 0.112	0.83	0.510 ± 0.020	0.20	0.796 ± 0.041	0.22	442
8	0.667 ± 0.026	0.30	0.478 ± 0.028	0.34	0.593 ± 0.034	0.13	442
9	0.500 ± 0.018	0.52	0.372 ± 0.029	0.42	0.448 ± 0.025	0.12	440
10	0.479 ± 0.027	0.85	0.329 ± 0.021	0.16	0.512 ± 0.056	0.04	434
11	0.389 ± 0.033	0.30	0.338 ± 0.013	1.21	0.457 ± 0.024	0.17	459
12	0.406 ± 0.027	0.84	0.321 ± 0.016	1.48	0.491 ± 0.024	0.28	442
13	0.414 ± 0.019	0.63	0.414 ± 0.030	1.06	0.480 ± 0.024	0.47	428
14	0.420 ± 0.029	0.77	0.328 ± 0.021	1.92	0.477 ± 0.025	0.32	431
15	0.439 ± 0.032	0.77	0.415 ± 0.029	1.30	0.434 ± 0.023	0.21	425
16	0.404 ± 0.045	0.98	0.371 ± 0.021	1.22	0.416 ± 0.022	0.22	410
17	0.407 ± 0.036	0.86	0.484 ± 0.046	1.03	0.386 ± 0.019	0.53	415
18	0.398 ± 0.020	0.94	0.474 ± 0.054	1.58	0.396 ± 0.021	0.20	411

Chapter 4

Discussion

The central question we pose in this work is whether the characteristic flickering frequency changes smoothly from its outburst value to its quiescent value, or whether the outburst value diappears and a separate, previously hidden quiescent value emerges. Dobrotka et al. (2016) identified a quiescent characteristic frequency near 0.4 mHz and additional outburst components near 1 mHz in V1504 Cyg. Similar characteristic frequencies were also found in the CV MV Lyr by Dobrotka et al. (2020). The authors comparison to other CV systems suggests that these frequency components may be common across CVs. Whether these components represent a single evolving source or multiple independent ones, however, remained unresolved. These two scenarios lead to fundamentally different interpretations of the flickering source geometry. In the first case, a single variability source evolves continuously as the disc transitions between states. In the second, multiple independent sources are present, each dominant in a different activity stage.

Both the PDS and AFP analyses yield a consistent answer: the frequency changes smoothly. No discontinuity is observed at any Bin. The quiescent and outburst signals are two states of the same component, not multiple independent sources. The rest of this chapter places this result in the context of the existing physical framework, discusses possible interpretations of what drives the frequency decline, and compares the two analysis methods.

4.1 Supporting Models

The outburst cycle of dwarf novae is well described by the DIM. During quiescence, observational evidence strongly supports the idea that the inner disc is truncated: the UV delay at outburst onset, the quiescent X-ray luminosity, and the suppression of inside-out outbursts all require the inner disc to be absent during the quiescent phase (Kimura & Yoji 2026). Flickering itself is most commonly interpreted within the fluctuating accretion disc model. Within this structure, the characteristic frequencies are set by the local viscous timescale at each radius, so that inner disc regions produce higher frequencies and outer regions produce lower ones. This general picture has been observed in CVs, X-ray binaries, and active galactic nuclei (Uttley et al. 2005; Arévalo & Uttley 2006; Scaringi 2014).

Several aspects of this framework, however, remain uncertain. The physical mechanism responsible for the inner disc truncation is not confirmed. The leading candidate is

evaporation of the thin disc material into a hot, optically thin, geometrically thick corona (Meyer & Meyer-Hofmeister 1994), which has recently been incorporated into numerical simulations of the DIM with promising results (Kimura & Yoji 2026). However, this has not been proven to be the only possible mechanism. Furthermore, while the fluctuating accretion disc model predicts that the highest frequencies originate at the smallest radii, the specific structure responsible for this variability is debated. Scaringi (2014) proposed that in MV Lyr the highest-frequency component is generated in the geometrically thick corona, but this is an interpretation of the model applied to a specific system, not a general conclusion. Finally, if the variability is generated in the corona, the optical signal should arise through reprocessing of the corona's X-ray emission by the thin disc. Dobrotka et al. (2020) showed that for MV Lyr the optical flickering flux exceeds the X-ray flux by approximately an order of magnitude, making this reprocessing scenario energetically insufficient. The exact mechanism by which the inner disc variability produces the observed optical signal therefore remains an open question.

Our results are consistent with the established parts of this framework. The smooth frequency decline from $\sim$1.8 mHz to $\sim$ 0.4 mHz traces the inner disc retreating outward as the system transitions from outburst to quiescence, as predicted by the combination of disc truncation and the fluctuating accretion disc model. The quiescent value of $\log(f_{\rm b}/{\rm Hz}) \approx -3.4$ matches the dominant break frequency found by Dobrotka et al. (2016) for V1504 Cyg in quiescence, and the peak frequency near $\log(f/{\rm Hz}) \approx -2.8$ matches the additional outburst break frequency found in the same paper. Our analysis confirms both the quiescent and outburst frequency values, while adding the previously missing information about how the transition between these two states proceeds. However, our data alone cannot resolve the open questions about the specific truncation mechanism or the radiative process connecting the inner disc variability to the optical signal.

4.2 Frequency Decline Origin

The smooth decline of the characteristic frequency during the outburst evolution implies that something is changing in the disc structure on the timescale of days. The physical mechanism driving this change, however, is not simple to identify. We explore two possible interpretations by comparing our observed frequencies with characteristic timescales in the disc.

Dynamical Timescale

We first test whether the observed frequencies could be of Keplerian origin, so, whether they correspond to the orbital frequency of disc material at some radius. The dynamical frequency is given by

$$f_{\rm dyn} = \frac{\Omega_K}{2\pi} = \frac{1}{2\pi}\sqrt{\frac{GM}{R^3}}, \tag{4.1}$$

from which we can obtain the radius corresponding to a given frequency:

$$R = \left(\frac{GM}{4\pi^2 f^2}\right)^{1/3}. \tag{4.2}$$

Adopting a typical white dwarf mass $M = 1\,M_\odot$, with the corresponding radius $R_{\rm WD} \approx 5.5 \times 10^8$ cm obtained from the mass-radius relation of Nauenberg (1972), the outburst peak frequency of 1.8 mHz maps to $R \approx 1.0 \times 10^{10}$ cm ($\approx 18\,R_{\rm WD}$), while the quiescent frequency of 0.4 mHz maps to $R \approx 2.8 \times 10^{10}$ cm ($\approx 50\,R_{\rm WD}$). These radii correspond to the mid-to-outer disc. For comparison, the numerical simulations of Kimura & Yoji (2026) find quiescent inner disc truncation radii of 3.9×10^9 cm for SS Cyg and 5.9×10^9 cm for U Gem, both significantly smaller. If the observed frequencies are of dynamical origin, the variability source would therefore be located in the outer half of the disc.

Viscous Timescale

An alternative is that the observed frequencies are set by the local viscous timescale. In the fluctuating accretion disc model, variability at each radius is generated by turbulent processes whose characteristic scale is set by the disc scale height H, the largest dimension over which coherent structures can form. The radial extent of a typical perturbation is therefore also of order $\sim H$, and the time for this perturbation to evolve or dissipate through the disc by viscous processes is $t_{\rm visc} \sim H/v_R$, where v_R is the radial drift velocity. The corresponding characteristic frequency is $f_{\rm visc} = 1/t_{\rm visc}$. Note that this differs from the global viscous timescale $\sim R/v_R$, which describes the time for matter to cross the entire disc from where it originated by viscous processes. Here, we are interested in the local variability timescale associated with individual perturbations at a given radius.

We computed both H and v_R as functions of radius using the standard Shakura–Sunyaev disc solution (Frank et al. 2002):

$$H = 1.7 \times 10^8\ \alpha^{-1/10}\,\dot{M}_{16}^{3/20}\,m_1^{-3/8}\,R_{10}^{9/8}\,F^{3/5}\ \ {\rm cm}, \tag{4.3}$$

$$v_R = 2.7 \times 10^4\ \alpha^{4/5}\,\dot{M}_{16}^{3/10}\,m_1^{-1/4}\,R_{10}^{-1/4}\,F^{-14/5}\ \ {\rm cm\,s^{-1}}, \tag{4.4}$$

where

$$R_{10} = R/(10^{10}\,{\rm cm}), \quad m_1 = M/M_\odot, \quad \dot{M}_{16} = \dot{M}/(10^{16}\,{\rm g\,s^{-1}}), \quad F = \left[1 - \left(\frac{R_{WD}}{R}\right)^{1/2}\right]^{1/4}.$$

These expressions describe a hot, fully ionized thin disc and are therefore valid only during outburst. As before, we adopted $m_1 = 1$, $R_{\rm WD} \approx 5.5 \times 10^8$ cm and an outburst mass accretion rate of $\dot{M} = 10^{-9}\,M_\odot\,{\rm yr^{-1}}$ ($\dot{M}_{16} \approx 6.3$; Frank et al. 2002), with the viscosity parameter α varied between 0.1 and 0.5.

Since the Shakura–Sunyaev solution applies only to the hot disc during outburst, we can only map the outburst peak frequency to a radius. The peak frequency of 1.8 mHz corresponds to $R \approx 2\,R_{\rm WD}$ for $\alpha = 0.1$ and $R \approx 4\,R_{\rm WD}$ for $\alpha = 0.5$. These are inner disc radii, consistent with the quiescent truncation radii found by Kimura & Yoji (2026).

Interpretation

The viscous timescale places the outburst frequency at radii consistent with the inner disc, while the dynamical timescale places it in the mid-to-outer disc. Both represent possible locations for the variability source, and each carries its own difficulties.

The inner disc interpretation is supported by the fact that the viscous radii are consistent with the truncation radii found by Kimura & Yoji (2026). However, their simulations also show that the inner disc edge remains at the white dwarf surface throughout the outburst. The cooling front must first propagate all the way inward through the disc before evaporation can begin, because ahead of the front, toward the centre, the disc is still hot and massive and does not evaporate. Only once the cooling front has reached the inner regions and the local accretion rate has dropped sufficiently does the evaporation rate exceed the accretion rate, which causes the inner disc to begin receding. This occurs near the very end of the outburst. In contrast, our observed frequency decline begins already at Bins 2–3, well before the outburst has ended. The smooth frequency evolution we observe during the outburst decline therefore does not correspond to the inner disc receding, at least not during the early and middle stages of the decline.

The mid-to-outer disc interpretation, suggested by the dynamical timescale, raises a different set of concerns. Most importantly, we do not know what structure could generate such variability at these radii. If the variability is connected to a structure in the outer disc, one candidate could be the cooling front itself. However, in the standard DIM, the cooling front originates only near the outer disc edge and propagates inward, while our frequencies decrease, suggesting outward motion. One possibility is that the cooling front can under certain conditions originate deeper within the disc, where it would then propagate inward and outward from its point of origin. Then, the outward-propagating component could potentially account for the observed frequency decrease. The questions why we would not see the inward-propagating component and whether a cooling front can even originate deeper in the disc remain open.

Neither interpretation provides a complete explanation with the present data. The viscous timescale yields consistent radii but an inconsistent evolution profile. The dynamical timescale yields radii in the mid-to-outer disc but lacks a clear source. Resolving these questions would require more detailed modelling of how the disc structure evolves during the outburst decline and how this affects the variability timescales.

4.3 Frequency Evolution

Beyond the overall smooth decline, the frequency evolution contains several features worth noting. In both the PDS and AFP, the characteristic frequency does not reach its maximum at the outburst peak itself (Bin 0), but rather around Bins 2–3, corresponding to approximately 0.5–0.75 d after the outburst maximum. One possible explanation is that the inner disc requires some time to fully rebuild after the heating front arrives, meaning that the highest characteristic frequencies are not reached when the disc is brightest but slightly later. This is consistent with the general observation that characteristic frequencies depend on the activity state of the disc rather than on the instantaneous flux (Dobrotka et al. 2016).

4.4 Comparison of the PDS and AFP Methods

The agreement between the PDS and AFP results is an important outcome of our work. The PDS is an established tool for characterizing variability, while the AFP method is less commonly used and has not previously been applied to such a degree as in this work. The fact that both methods recover the same behaviour, a smooth decline from a peak frequency to a quiescent one over approximately 2 days, validates the use of the AFP as an independent approach to the PDS. The decline visible in the PDS is unambiguous on its own, but the two Bins preceding the peak carried larger uncertainties and required independent verification. The AFP confirms the same evolution in these Bins and strengthens the overall result.

Characteristic Frequencies

Comparing f_r and f_d with f_b in Fig. 4.1, it is clear that both f_r and f_d are systematically lower than f_b during the outburst Bins, converging only in quiescence. In previous applications of the AFP method, the characteristic timescales extracted from the flare profile matched the corresponding PDS frequencies well. This was demonstrated by Negoro et al. (2001) for the X-ray binary Cyg X-1, and by Dobrotka et al. (2019) for the CV MV Lyr. The systematic offset observed in our data (by a factor of ~ 2) is, to our knowledge, the first instance where the AFP frequencies do not align with the PDS break frequency during the high state. The cause of this discrepancy is unclear and may warrant further investigation.

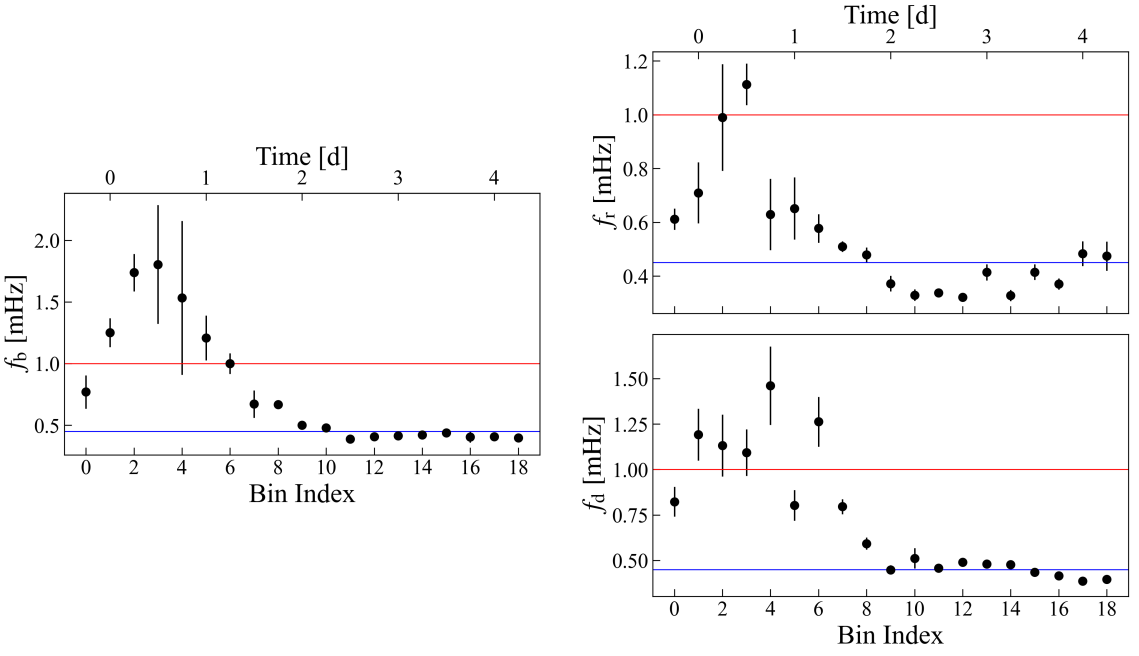

Figure 4.1: Comparison of the characteristic frequencies derived from the PDS and AFP analyses. The left panel shows the PDS break frequency f_b, the top right panel shows the AFP rise frequency f_r, and the bottom right panel shows the AFP decline frequency f_d. All values are plotted in mHz. The horizontal blue and red lines mark the reference quiescent frequency of 0.4 mHz and the frequency of 1.0 mHz, respectively.

Flare Morphology

Beyond the characteristic frequencies, the AFP reveals the shape of the variability structures themselves, information that is not accessible through the PDS. As described in Chapter 3, the flare profiles evolve systematically across the outburst, changing in width, amplitude and functional shape. The profiles also exhibit a consistent asymmetry between the rise and decline branches, most pronounced in the early outburst Bins, where $f_{\rm d} > f_{\rm r}$. The physical origin of both the morphological evolution and the branch asymmetry is not clear from the present analysis. A detailed physical model of the small-scale processes operating in the accretion disc would be needed to interpret these features.

Chapter 5

Summary

In this work, we analysed the evolution of the characteristic flickering frequency of the dwarf nova V1504 Cyg during the transition from outburst to quiescence, using photometric data from the *Kepler* satellite in short-cadence mode. Out of 118 detected normal outbursts, 112 were selected for analysis after excluding short outbursts and outbursts with data gaps near maximum. The lightcurve of each outburst was divided into 19 Bins of 0.25 d, spanning from the outburst maximum to 4.5 d into quiescence. Two independent methods were applied to extract characteristic frequencies from the flickering signal in each Bin, the PDS method and the AFP method.

The PDS analysis, based on Lomb–Scargle periodograms fitted with broken power law models, yielded a break frequency $f_{\rm b}$ that decreases smoothly from $\sim$1.8 mHz near 0.5–0.75 d after the outburst maximum to $\sim$0.4 mHz by approximately 2 d after maximum, where it remains for the rest of the analysed window. The quiescent value is in agreement with the break frequency reported by Dobrotka et al. (2016) for the same system.

The AFP analysis, using a linear-exponential flare model, yielded separate rise and decline frequencies ($f_{\rm r}$ and $f_{\rm d}$) that show the same smooth decline as $f_{\rm b}$. The agreement between the two methods validates the AFP as a complementary approach to the PDS for tracking frequency evolution. It was noted that both $f_{\rm r}$ and $f_{\rm d}$ are systematically lower than $f_{\rm b}$ during the outburst Bins, which is, to our knowledge, the first such observation in applications of the AFP method.

The smooth frequency evolution answers the central question of this work: the characteristic frequency changes continuously from $\sim$1.8 mHz to $\sim$0.4 mHz, rather than one component disappearing and another emerging. This indicates that a single variability source evolves as the disc transitions between states.

The physical mechanism driving the frequency decline remains an open question. A comparison with the dynamical timescale showed that the observed frequencies correspond to mid-to-outer disc radii, while a viscous timescale calculation placed the outburst peak frequency at inner disc radii of a few $R_{\rm WD}$, consistent with truncation radii found in recent simulations of the DIM (Kimura & Yoji 2026). However, these simulations also show that the inner disc edge does not begin to recede until the very end of the outburst, whereas our observed frequency decline begins much earlier. The viscous interpretation therefore yields consistent radii but an inconsistent evolution profile. What drives the smooth frequency decline while the inner disc is still in place, and whether the mid-to-outer disc plays a role in the observed variability, could not be determined from the present data alone.

Bibliography

Arévalo, P. & Uttley, P. 2006, MNRAS, 367, 801

Astropy Collaboration, Price-Whelan, A. M., Lim, P. L., et al. 2022, ApJ, 935, 167

Astropy Collaboration, Price-Whelan, A. M., Sipőcz, B. M., et al. 2018, AJ, 156, 123

Astropy Collaboration, Robitaille, T. P., Tollerud, E. J., et al. 2013, A&A, 558, A33

Balbus, S. A. 2005, in Proceedings of ASP Conference, ed. J. M. Hameury & J. P. Lasota, Vol. 330, 185

Balbus, S. A. & Hawley, J. F. 1998, Reviews of Modern Physics, 70, 1

Bartlett, M. S. 1948, Nature, 161, 686

Borucki, W. J., Koch, D., Basri, G., et al. 2010, Science, 327, 977

Chen, W., Shrader, C. R., & Livio, M. 1997, ApJ, 491, 312

Deeter, J. E. & Boynton, P. E. 1982, ApJ, 261, 337

Dobrotka, A., Negoro, H., & Bezák, P. 2024, A&A, 692, A94

Dobrotka, A., Negoro, H., & Konopka, P. 2020, Astron. Astrophys., 641, A55

Dobrotka, A., Negoro, H., & Mineshige, S. 2019, A&A, 631, A134

Dobrotka, A., Ness, J.-U., & Bajčičáková, I. 2016, Mon. Not. R. Astron. Soc., 460, 458

Done, C., Gierliński, M., & Kubota, A. 2007, Astron. Astrophys. Rev., 15, 1

Downes, R. A., Webbink, R. F., Shara, M. M., et al. 2001, PASP, 113, 764

Frank, J., King, A., & Raine, D. J. 2002, Accretion Power in Astrophysics: Third Edition

Ji, H., Burin, M., Schartman, E., & Goodman, J. 2006, Nature, 444, 343

Kimura, M. & Yoji, O. 2026, Disk instability model incorporating a variable inner disk radius in SS Cyg and U Gem

Knigge, C., Baraffe, I., & Patterson, J. 2011, Astrophys. J. Suppl. Ser., 194, 28

Kotov, O., Churazov, E., & Gilfanov, M. 2001, MNRAS, 327, 799

Lasota, J.-P. 2001, New Astron. Rev., 45, 449

Lyubarskii, Y. E. 1997, MNRAS, 292, 679

Meyer, F. & Meyer-Hofmeister, E. 1994, A&A, 288, 175

Narayan, R. & Yi, I. 1995, ApJ, 452, 710

Nauenberg, M. 1972, ApJ, 175, 417

Negoro, H., Kitamoto, S., & Mineshige, S. 2001, Astrophys. J., 554, 528

Negoro, H., Miyamoto, S., & Kitamoto, S. 1994, ApJL, 423, L127

Osaki, Y. 1974, Publications of the Astronomical Society of Japan, 26, 429

Osaki, Y. & Kato, T. 2014, Publications of the Astronomical Society of Japan, 66, 15

Papadakis, I. E. & Lawrence, A. 1993, MNRAS, 261, 612

Rappaport, S., Joss, P. C., & Webbink, R. F. 1982, ApJ, 254, 616

Scargle, J. D. 1982, ApJ, 263, 835

Scaringi, S. 2014, Mon. Not. R. Astron. Soc., 438, 1233

Schreiber, M. R., Hameury, J.-M., & Lasota, J.-P. 2003, Astron. Astrophys., 410, 239

Seabold, S. & Perktold, J. 2010, in 9th Python in Science Conference

Shakura, N. I. & Sunyaev, R. A. 1973, A&A, 24, 337

Smak, J. 2000, New Astronomy Reviews, 44, 171

Smak, J. I. 1998, Acta Astronomica, 48, 677

Spruit, H. C. & Ritter, H. 1983, A&A, 124, 267

Uttley, P., McHardy, I. M., & Papadakis, I. E. 2002, MNRAS, 332, 231

Uttley, P., McHardy, I. M., & Vaughan, S. 2005, MNRAS, 359, 345

van der Klis, M. 1989, in NATO Advanced Study Institute (ASI) Series C, Vol. 262, Timing Neutron Stars, ed. H. Ögelman & E. P. J. van den Heuvel, 27

Vaughan, S., Edelson, R., Warwick, R. S., & Uttley, P. 2003, MNRAS, 345, 1271

Virtanen, P., Gommers, R., Oliphant, T. E., et al. 2020, Nature Methods, 17, 261

Warner, B. 1995, Cataclysmic variable stars, Vol. 28